McKelvey School of Engineering Theses & Dissertations

McKelvey School of Engineering

Summer 8-18-2016

Development and Evaluation of a Near-infrared (1047 nm) Photoacoustic-Nephelometer Spectrometer for Detection and Optical Characterization of Black Carbon Aerosol

Yang Yu
Washington University in St Louis

Follow this and additional works at: https://openscholarship.wustl.edu/eng_etds

Part of the Nanoscience and Nanotechnology Commons

WASHINGTON UNIVERSITY IN ST. LOUIS

School of Engineering and Applied Science

Department of Energy, Environmental and Chemical Engineering

Thesis Examination Committee:

Dr. Rajan K. Chakrabarty, Chair

Dr. Pratim Biswas

Dr. Richard L. Axelbaum

Development and Evaluation of a Near-infrared (1047 nm) Photoacoustic-Nephelometer

Spectrometer for Detection and Optical Characterization of Black Carbon Aerosol

by

Yang Yu

A thesis presented to the School of Engineering

of Washington University in St. Louis in partial fulfillment of the

requirements for the degree of

Master of Science

August 2016

Saint Louis, Missouri

Contents

List of Figures

List of Tables

Acknowledgments

This dissertation would not have been possible without the help and support from the members in the Chakrabarty laboratory. I dedicate this part to those who have provided advice and help to my research and accompanied me for the past two years.

First, I am grateful to my advisor, Professor Rajan K. Chakabarty. Thank you for providing me the opportunity to become a Master of Science student and research assistant in your group. It was a pleasure joining your team. Your guidance, support and encouragement enabled me to develop an interest and understanding of the photoacoustic technique and its application to aerosol science. Your enthusiasm and keen interest guided me with my research direction. Your intelligent advice and critical insight inspired me in my research process and also my future development.

Also, I would like to thank all members in Chakrabarty's group past and present, for providing support and assistance though my research. I especially thank to Pai Liu, for helping me get started the research in our lab and my projects afterwards. Your prompt inspiration, timely suggestions, enthusiasm, and dynamism enabled me to become a real researcher who can think and solve problems. You are also my best friend in Washington University. I would like to thank Ian Arnold for the guidance and help me to get started with the 1057nm-Photoacoustic system building and aerosol optical properties measurements. Thanks to Benjamin Sumlin for discussion and assistance on Photoacoustic maintenance and measurement. Thanks to Apoorva Pandey for help with UV-vis and filter sample study. Thanks

to Dr. William Heinson, Bongjin Seo, Zhihong Guo, Bo Huang and Thomas Hildebrand, for the discussions related to laboratory experiments and life.

I would like to thank Yining Ou, Yang Wang, Jiayu Li, Wei Yang, Wei Bai, Dapeng Ding and Cheng-en Sung. Your collegial guidance and support help me overcome troubles from academic life in WUSTL. I thank all the people, who assisted but are not specifically named here.

I also want to thank my girlfriend Yi Li, for her encouragement and accompany throughout years. Thank you for your endless love, trust and the understanding. Thank you for all the comfort and encouragement when I want to give up. I love you!

Finally, I want to thank my parents. They give the birth and all their love to me. Without their love and financial support, I won't be able to finish my degree in WUSTL. I love you!

ABSTRACT OF THE THESIS

Development and Evaluation of a Near-infrared (1047 nm) Photoacoustic-Nephelometer

Spectrometer for Detection and Optical Characterization of Black Carbon Aerosol

By

Yang Yu

Master of Science in Energy, Environmental and Chemical Engineering

Washington University in St. Louis, 2016

Research Advisor: Professor Rajan K. Chakrabarty

Black carbon (BC) aerosol are aggregates of small carbon spherules of <10 nm to approximately 50 nm in diameter. They are characterized by their strong visible light absorption property with a mass absorption cross-section (MAC) value above 5 m^2 g^{-1} at a wavelength $\lambda = 550$ nm, which increases inversely with wavelengths from near-infrared (≈ 1 μm) to ultraviolet with a power law of one. The absorbing nature of BC aerosol has been implicated in regional atmospheric warming, changing of monsoon patterns, and accelerated melting of the glaciers. The BC radiative effects over earth is currently estimated within a factor of four, resulting in one of the largest uncertainties in climate modeling. This uncertainty results from our inadequate knowledge about regional BC emission rates, and associated aerosol microphysical properties. Conventional methods for quantifying BC mass concentration in the atmosphere are filter-based techniques, which have limitations with respect to dynamic range, lack of a common definition of BC, and scattering aerosol

interferences during measurement. Contact-free measurement techniques such as Photoacoustic spectroscopy and nephelometry overcome these deficiencies associated with filter-based sampling methods.

This thesis discusses the design and development of a novel, integrated photoacoustic-nephelometer (IPN) spectrometer operating at 1047 nm wavelength for accurate detection and measurement of BC aerosol. Choice of this wavelength was made because of minimal gaseous interference and availability of a high-power laser source that allowed for direct electronic modulation of the power at the resonator acoustic frequency. Simultaneous measurement of light scattering by reciprocal nephelometry within the photoacoustic resonator cell facilitates measurement of aerosol absorption (β_{abs}) and scattering (β_{sca}) coefficients at 1 Hz frequency. The principles behind instrument operation is described in detail. Also described and implemented is a robust method of instrument calibration and stability analysis using the Allan deviation method. The Allan deviations for β_{abs} and β_{sca} were estimated to be 0.14 and 3.42 Mm^{-1}, respectively. The 2σ (two standard deviation) values, which are considered to be the detection limit for a 10-min averaged β_{abs} and β_{sca} measurements, were 1.15 and 40.14 Mm^{-1}, respectively. The potential performance of this instrument at lower pressure environments (such as on aircrafts) was also evaluated. Finally, this instrument was used to measure the MAC and mass scattering cross-sections (MSC) values of BC aerosols. The measurement results were in good agreement with theoretical predictions.

1　Introduction to Black Carbon

1.1　What is Black Carbon?

Black carbon (BC), often called "soot", is a distinct type of carbonaceous particular matter that is formed particularly during combustion[1]. It is directly emitted to the atmosphere and can be found throughout the earth's environment system. BC plays a unique and significant role in the climate system because it absorbs solar radiation, thus impact the melting process of snow and ice and the formation of clouds. In measurement and modeling studies, the use of "black carbon" has not been limited to materials with these properties, causing a lack of comparability among results. Many methods used to measure the properties of black carbon can be biased by the presence of other chemical components[2]. For example, the mass concentration value, based on different methods can vary by 80%.

Previous studies have shown large differences between estimates of the effect of BC on climate, but the reasons behind these differences are not well understood. As a preliminary to further discussion, this chapter provides a comprehensive introduction to black carbon's properties, categories, constitution, and climate impacts.

1.2　History of Black Carbon Analysis

In 1967, McCormick and Ludwig suggested that aerosols could influence the climate[3]. After that, Charlson and Pilat pointed out that aerosol light absorption may cause warming rather

than cooling in 1969. Hidy's Pasadena Smog Experiment and Aerosol Characterization Experiment were important milestones in the development of aerosol research[4].

In 1972, Mueller et al. showed that carbon comprised a substantial fraction of sub-micron Pasadena aerosol particles[5]. Later on, in 1973, Friedlander developed the first carbon balance for Pasadena aerosol, and he concluded that directly emitted carbon particles from petroleum powered transportations were mostly organic compounds with small portion of elemental carbon[5]. Black carbon was first isolated in urban pollution, when Rosen et al. found that refractory, graphitic particles were responsible for light absorption. As a result, black carbon appeared, at the time, to be a minor constituent of big city smog aerosol[6].

The indications that BC might be a significant part of urban air pollution aerosols motivated investigations to characterize and measure of BC aerosols. In 1973, Lin et al. published a method for light absorption measurement by measuring the transmission of green light through the aerosol layer collected on a transparent (nuclepore) filter[7]. Later on, in 1978, Rosen et al. employed a different method, using millipore and quartz filters for particle collection and a He–Ne Laser as the light source to measure the aerosol light absorption[6]. Yasa et al. reported results of black carbon characterization using a photoacoustic technique, which gave an independent demonstration of the light absorption by graphitic carbon in 1979[8].

In the 1980s, several analytical methods were invented to separate black from organic carbon. One technique, reported by Dod and Novakov, known as evolved gas analysis (EGA), also heats a sample on a quartz filter at a constant rate in an oxidizing atmosphere of O_2 and neutral N_2[9]. After that, Huntzicker et al. developed an instrument based on the volatilization

of organic carbon (OC) from the filter at temperatures where the elemental carbon remains intact. The volatilized carbon is oxidized to CO_2, reduced to CH_4, and measured by a flame ionization detector. Elemental carbon is subsequently oxidized to CO_2 and measured. The reflectance of the laser beam by the filter is continuously monitored to correct for charring artifacts[10]. As a result of these developments in 1980s, BC was defined as the highly absorbing component of soot having a graphitic microstructure.

A variant of the thermal/optical reflectance apparatus for carbon analysis was built by Chow et al. in 1993, and they were used to analyze more than 27,000 samples from variety of urban and regional air quality studies in the USA. In this apparatus, a portion of the sample is exposed to a series of temperatures in a pure helium atmosphere, followed by oxidation at several temperature settings in a 2 % oxygen and 98 % helium atmosphere. The carbon content of gases that evolves at each temperature is converted to methane and quantified with a flame ionization detector[11].

Recently, advanced aerosol technologies capable of single particle detection and in situ measurement of aerosol properties with high time resolution have been developed. In 2009, Jimenez et al. presented a combination modeling and measurement study on organic aerosols using an aerosol mass spectrometer (AMS)[12].

Most of the developments mentioned above relate to air quality in urban atmospheres. The first indications of the role of BC in a larger global context came from studies of the Arctic Haze phenomenon. Analyses of filter-collected samples by Rosen et al. from 1981 to 1984 showed surprisingly large BC concentrations throughout the Arctic troposphere[13, 14]. From the analysis of the collected data, they concluded that the absorbing component of the Arctic

Haze was come from high temperature combustion, presumably from anthropogenic sources, because the only other contributor could be forest fires, which should be negligible. Recent measurements of BC at ground level stations and from aircraft in the Arctic have shown a downward trend compared to the BC values in the 1980s. These downward trends have been attributed to reduced emissions in northern Eurasia. BC in the snow has been recently measured by Doherty et al.[15]. These values are, within experimental error, similar to those found in the 1980s. As energy use increases dramatically in the next several decades, the future trends of BC in the Arctic and elsewhere will depend on the mix of combustion technologies and the fuel mix used to support this energy growth.

An important milestone in the realization of the importance of black carbon was the 1st International Conference on Carbonaceous Particles in the Atmosphere, held at Lawrence Berkeley National Laboratory in 1978. Its organization reflected the view of a number of early participants in the aerosol field that carbonaceous particulate material may be a very important component of atmospheric aerosols, with implications for atmospheric chemistry and physics, climate, air quality, and public health. This conference was followed by a series of ten international conferences on carbonaceous particles in the atmosphere, held alternatively in the US and in Austria. In 2000, a number of papers pointed out that black carbon may bear one-third as much responsibility as CO_2 for atmospheric warming[16-18].

1.3   Physical and Chemical Properties of Black Carbon

Black carbon is formed by incomplete combustion of carbon-based fuels. It is distinguishable from other forms of carbon compounds in the atmosphere because it has a unique combination of physical properties:

1. Black carbon strongly absorbs visible radiation, with a mass absorption cross-section (MAC) of at least 5 m^2g^{-1} at 550 nm[19].

2. It is refractory, which means black carbon can endure high temperature, and its vaporization temperature near 4000K[20].

3. Black carbon is insoluble in water, in several organic solvents (such as acetone and methanol) and in other components of atmospheric aerosols[21].

4. Black carbon commonly presents as a chain aggregate of elemental spherical carbon particles.

Among all physical properties, strong absorption of visible light is the distinctive characteristic for black carbon. No other aerosol in the atmosphere in significant quantities has such strong light absorption per unit mass. This unique property has raised the interest of many scientists investigating atmospheric radiation transfer.

Although black carbon has very low chemical reactivity in the atmosphere, for impure black carbon, various functional groups exist on the surface. Oxidizing black Carbon, with a large amount of hydroxyl groups gives it a greatly enhanced utility in print inks or varnishes, showing excellent dispersibility.

1.4 Sources of Black Carbon

BC is generated from both natural and anthropogenic sources. Fig. 1.1 shows the multi-faceted interaction of black carbon with the environment. Burning of forests and savannas, solid fuel burning for cooking and heating, and combustion by diesel engines are the largest global sources. Industrially generated black carbon is also a significant fraction of global black carbon emission, while, aviation and shipping emissions, are minor contributions. After being emitted, black carbon undergoes regional and internationally transported by the atmosphere and finally deposited on the ground. The average atmospheric lifetime for black carbon is about a week.
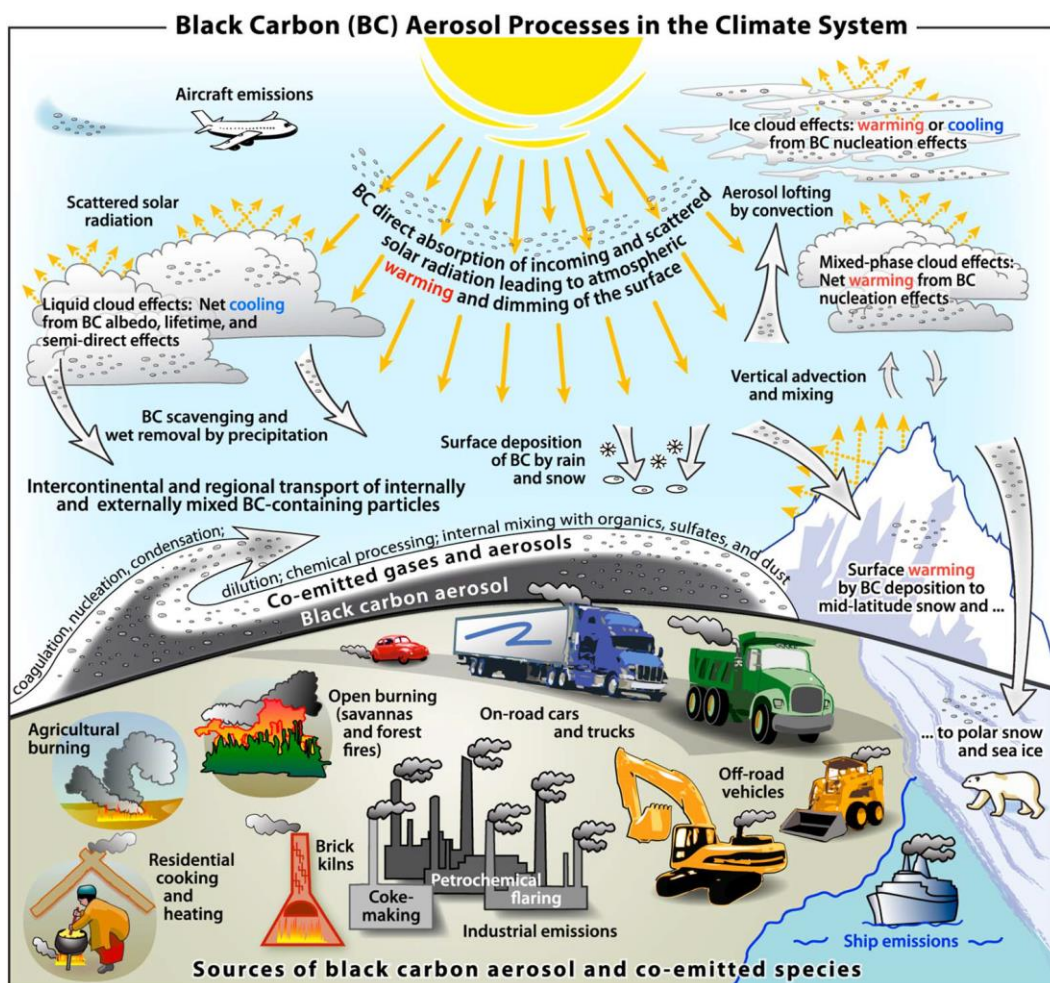
Figure 1.1 Overview of the primary black carbon emission sources and the processes that control the distribution of black carbon in the environment[2]

In the year 2000, global black carbon emissions were estimated to be 7500 Gg yr^{-1}, using bottom-up inventory methods[2]. The primary sources of black carbon are shown in Fig 1.2. As mentioned, although a variety of sources generate black carbon, there is an agreement that the three largest contributors are open biomass burning, transport, and domestic/residential solid fuel burning. In the US, transport is the main source, while cooking is a major source in India.

Global Black Carbon Sources

0.5%
19.3%
35.5%
25.1%
19.0%
0.7%

U.S. Black Carbon Sources

1.0%
3.6%
1.1%
6.8%
35.3%
52.3%

■ Open Biomass Burning   ■ Transport

■ Energy/Power   ■ Domestic/Residential

■ Industry   ■ Other
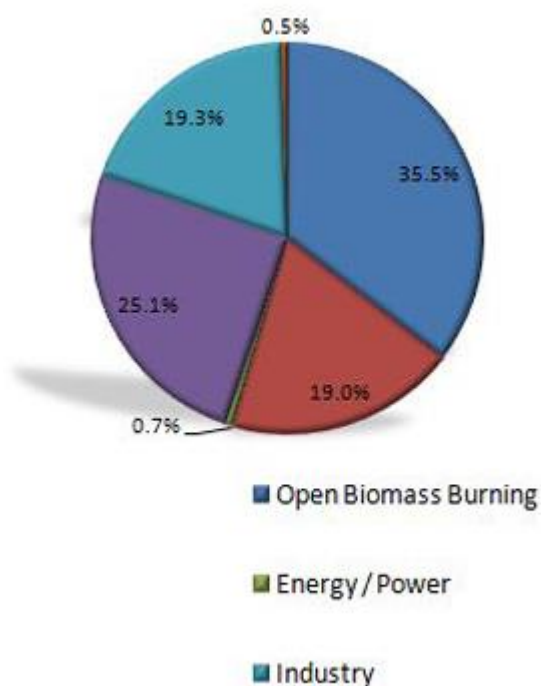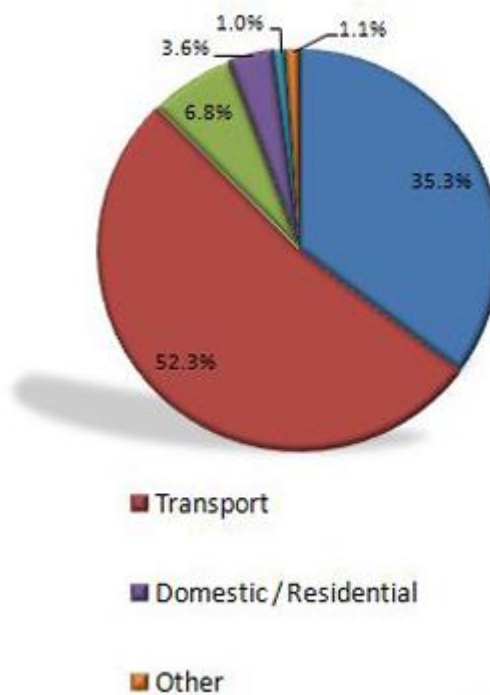
U.S. EPA Data

Figure 1.2 The primary sources of black carbon emissions in globally and in the US (2010)

The difficulty in quantifying emissions from such diverse sources contributes to uncertainty in analyzing black carbon's climatic role. In 2000, Novakov et al. reported a method using the ratio of total carbon to black carbon in aerosols to classify black carbon sources[17].

Another method was reported by Brodowski et al., who distinguish source-based differences in shapes, sizes, surface properties, and partial oxidation of the black carbon aerosols from vegetation fire and coal combustion sources[22].

1.5 Categories of Black Carbon

BC particles, formed from random collisions between dispersed monomers, have random shapes. The structure of BC particles was described as "fluffy" or "grainy", have been known for years. This fractal geometry was first reported by Mandelbrot in 1975[23].

BC fractal structures present repeating branching structures, like the toy model of a tree shown in Fig.1.3. It first starts with the trunk rising from the ground, then split into two branches; those two branches continue and at some point split again to four branches, and repeat this process. The tree looks the same at all length scales, if you were to break off a twig from this model tree and compare it to the whole, a zoomed-in view of the twig would look like the entire tree[24]. The particles composing the aggregates are called "monomers" or "primary particles". Ideally they are spherical with point contacts and are all the same size, but this description is an approximation[25]
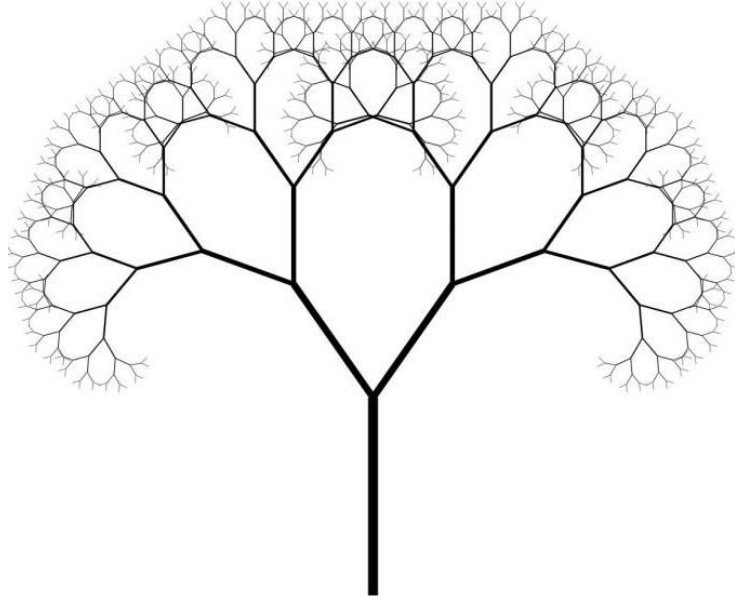
Figure 1.3 Example of model tree with a fractal structure

The fractal structure of BC is described by the mass-radius scaling law:

$$N = k_0 (\frac{R_g}{a})^{D_f},$$ (1.1)

where N is the number of monomers of a given radius in the BC, also refer as the "mass" of

the BC fractal aggregate. R_g is the radius of gyration of BC fractal aggregate, which is a

measure of its linear size and it is defined as root-mean-square radius. D_f is the fractal

dimension, a value less than the spatial dimension, d. k_0 is the scaling prefactor. Equation

(1.1) is considered to be the defining relationship for fractal aggregates[26]. From equation (1.1),

we can obtain

$$R_g \sim N^{(1/D_f)}.$$ (1.2)

The mean nearest neighbor separation R_{nn} is controlled by the spatial dimension, d. It is

related to total number of clusters N_c in a system of volume V by

$$R_{nn} \sim (N_c/V)^{-(1/d)}.$$ (1.3)

In a mass conserving system, the total number of monomers, N_m, in the system is constant.

Under the assumption that the aggregates have the same size, we get

$$N_m = N_c N. \tag{1.4}$$

Then, substituting equation (1.4) into equation (1.3), we get

$$R_{nn} \sim N^{1/d}. \tag{1.5}$$

Typically, in a given particle, the aggregates are far apart relative to their average nearest

neighbor separations, i.e., $R_{nn} \gg R_g$. However, as aggregation proceeds, as described by the

increasing cluster mass N, equations (2) and (5) show that since $d > D_f$, R_g increases faster

than R_{nn} and eventually catches up with it. When it does, i.e., when $R_{nn} \sim R_g$, the system gels

(see below), as mentioned by Kolb et al[27]. and Vicsek[28]. Thus, simply said, systems gel

because $D_f < d$, as displayed in Fig. 1.4.
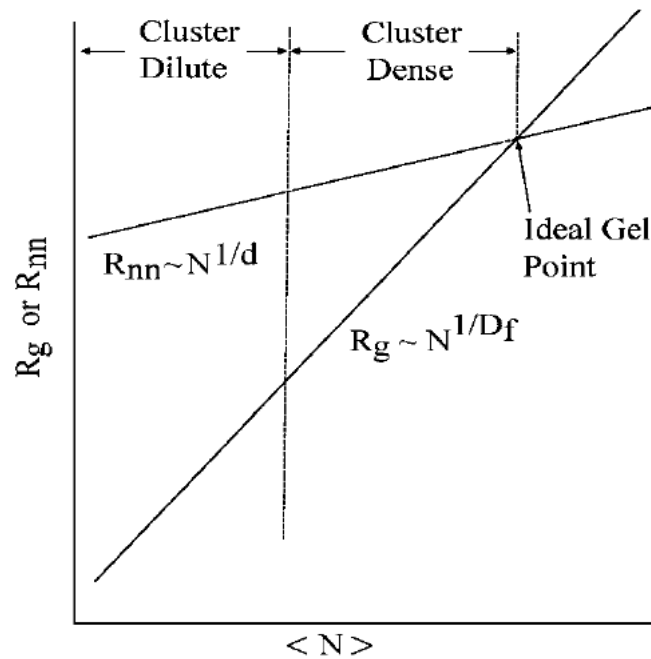
Figure 1.4 The evolution of the two primary length scales in an aggregating sol versus the mean number of monomers per aggregate <N>[29]

The length scales are the aggregate radius of gyration, R_g, and the aggregate mean nearest neighbor separation, R_{nn}. The functionalities of these length scales are governed by the aggregate fractal dimension, D_f, and the spatial dimension, $d > D_f$. Cluster dilute ($R_{nn} \gg R_g$) and cluster dense ($R_{nn} \geq R_g$) regimes are indicated. The ideal gel point is when these two length scales are approximately equal.

Fig. 1.4 sketches the behavior of R_g and R_{nn} as a function of the mean number of monomers per aggregate <N>, which grows with time as the aggregation proceeds. When $R_{nn} \gg R_g$, the aggregates are relatively very far apart, a condition we call cluster dilute. As aggregation proceeds, both R_{nn} and R_g grow, but the relative cluster separation R_{nn}/R_g decreases with time. Below we show that when this ratio decreases to about 10, changes occur in the aggregation kinetics due to cluster crowding. Thus the system enters what we call the cluster dense regime. These two regimes are identified in Fig. 1.4. Well into the cluster dense regime, the aggregates grow to the point that they fill the entire system volume. Then neighboring clusters touch and the cluster volume fraction equals one. We define this point as the ideal gel point. Its approximate condition is when $R_{nn} \sim R_g$, as indicated in Fig. 1.4. Beyond the ideal gel point, the fractal clusters interdigitate. Eventually a system spanning cluster forms, marking the physical gel point. Continued aggregation after the gel point involves incorporation of the remaining material into the spanning gel until every monomer is part of the same network, a point called the final gel state.

In this study, the black carbon aggregates' D_f is 1.8, and the aggregate forms in the cluster dilute regime, while the fractal dimension for black carbon percolated aggregates is 2.6, and

the particles are form after the ideal gel point. Further discussion will be provided in the results and discussion section.

1.6 Black Carbon's Climatic Impact

BC impacts the formation of clouds, snow, and ice. After emission, black carbon is mixed with other aerosol components in the air during its transportation. This process increases its light absorption, its ability to form liquid cloud droplets and ice nuclei, and its atmospheric removal rate.

Black carbon changes the number of liquid cloud droplets and enhances precipitation in mixed-phase clouds, changing their ice particles as well as influencing the extent of the cloud. These direct effects cause a radiative change in the clouds, an indirect effect of black carbon. However, light absorbed by black carbon alters the temperature structure inside or outside of the clouds and finally change the cloud distribution, a semi-direct effect.

The best estimate of industrial-era climate change from black carbon cloud effects is positive, with substantial uncertainty (+0.23 Wm^{-2}, with a -0.47 to 1 Wm^{-2} 90% uncertainty range). Very few climate model studies have isolated the influence of black carbon in these indirect effects.

Black carbon deposited on ice and snow alters the radiative forcing, the snow-albedo feedback. The combination of all these effects causes positive climate forcing. The best estimation of climate forcing from black carbon deposition on snow and ice in the industrial era is +0.13 Wm^{-2}, with 90% uncertainty bounds of +0.04 to +0.33 Wm^{-2}. The estimated

all-source present-day climate forcing, including preindustrial emissions, is higher than +0.16

Wm^{-2}. The enhanced climate feedback is included in the +0.13 Wm^{-2} forcing estimate[2].

1.7   Black Carbon's Optical Properties

Fundamental optical properties, such as absorption and scattering coefficients (m^{-1}), are

important in evaluating the environmental impact of BC. Absorption and scattering per mass

of BC are described as the mass absorption cross section (MAC) and mass scattering cross

section (MSC), respectively. Ideally, we would know these values at all wavelengths. A

comprehensive review of black carbon's optical properties has been given by Bond and

Bergstrom, suggesting a refractive index of 1.95+0.79i and a mass absorption efficiency of

7.5 ± 1.2 m^2/g at 550 nm[2].

From field measurements, MAC can be calculated as the absorption coefficient (β_{abs}) divided

by the mass concentration. Throughout this method, we often refer to MAC that is

determined for BC alone (MAC$_{BC}$). MAC$_{BC}$ is calculated by dividing the absorption

coefficient attributable to BC by the BC mass concentration. The simple term MAC indicates

the value determined by the β_{abs} divided by the total mass concentration of BC-containing

particles, which is smaller than the MAC$_{BC}$ value. All other properties are usually measured

for BC-containing particles, not for pure BC. Optical properties depend on refractive index,

density, size distribution, mixing state, and particle shape. The percentage of water absorbed

in the BC-containing particles affects the MSC and MAC values, as well as the particles'

ability to form cloud droplets, and their atmospheric lifetime due to removal by precipitation.

For sub-saturated conditions (relative humidity below 100%), this water uptake capability is characterized in terms of hygroscopicity or the growth factor[30].

The MAC was mentioned earlier as a distinguishing feature of BC. Values of MAC and MSC are fundamental inputs to the radiative transfer models which were required for all aerosols or aerosol components. These quantities are necessary to translate mass concentrations simulated by chemical transport models to their effects on radiative transfer. The wavelength dependence of MAC must also be represented in models for the full solar spectrum. BC strongly absorbs light at all visible wavelengths. The quantity generally used to characterize the spectral dependence of light absorption is the absorption Angstrom exponent, and it is expressed as

$$\text{Å} = \frac{-\log(\frac{MAC(\lambda_1)}{MAC(\lambda_2)})}{\log(\frac{\lambda_1}{\lambda_2})}, \tag{1.6}$$

where $MAC(\lambda_1)$ and $MAC(\lambda_2)$ are the mass absorption cross sections at wavelengths λ_1 and λ_2. Another way to calculate Å is to use β_{abs} data at two different wavelengths instead of MAC values. The value of Å for particles is usually greater than that of the bulk material. If the refractive index of the bulk material has no wavelength dependence, e.g., graphite[31], then $\text{Å}_{abs}=1$ for particles much smaller than the wavelength of light[32].

Measurement studies have confirmed the value of Å = 1 for BC domain particles[6, 33, 34]. When BC particles are coated by other components, Å can vary in the range of 0.8 to 1.9[35]. In contrast, Å for organic aerosols are reported between 3.5 to 7[34, 36, 37]. Å for dust is normally about 2 to 3 but can be higher for iron-rich dust[33]. This difference in the wavelength dependence of

absorption by BC versus other absorbing aerosols has been used to approximate relative fractions of BC versus other light-absorbing constituents.

The single scattering albedo (ω) is another distinguishing feature of BC containing particles. It is expressed as

$$\omega = \frac{MSC}{(MSC + MAC)}. \tag{1.7}$$

The MAC and MSC can also be replaced by β_{abs} and β_{sca}. A value of ω close to 1 illustrates that an aerosol is mainly scattering. When ω is lower than 0.8, the particles could have a warming effect on climate[38].

The value that divides warming from cooling also depends on the albedo of the underlying surface or clouds and the fraction of light that is scattered upward by the particles[39]. When the addition of aerosol causes a local increase in the planetary albedo, more shortwave radiative energy is reflected back to space, and aerosol exerts a negative forcing. In contrast, when aerosols locally decrease the planetary albedo, the forcing is positive. MAC and ω are the aerosol properties most relevant to the balance between negative and positive forcing, so we emphasize these two parameters in this section instead of MSC. Forcing is not very sensitive to ω for strongly absorbing aerosols with values below 0.4.

1.8 Framework and Motivation of This Study

1.8.1 Objectives

Black carbon (BC) aerosol strongly absorbs visible light. The absorbing nature of BC aerosol have been implicated in regional atmospheric warming, changing of monsoon patterns, and accelerated melting of the glaciers. The BC radiative effects over earth is currently estimated within a factor of four, resulting in one of the largest uncertainties in climate modeling. This uncertainty results from our inadequate knowledge about regional BC emission rates, and associated aerosol microphysical properties. Conventional methods for quantifying BC mass concentration in the atmosphere are filter-based techniques, which have limitations with respect to dynamic range, lack of a common definition of BC, and scattering aerosol interferences during measurement. Contact-free measurement techniques such as Photoacoustic spectroscopy and nephelometry overcome these deficiencies associated with filter-based sampling methods.

1.8.2 Project Frame Work and Significance

The author's specific contribution to this large study was the construction of an integrated photoacoustic-nephelometer (IPN) spectroscopy with a 1047 nm laser. Laser aligned and calibrated to assure the accuracy. Before using the IPN spectrometers to measure the optical properties of aerosols, its signal stability (using the overlapping Allan deviation method) and detection limit were evaluated. Next, to test the accuracy for aloft measurements, instrumental data at different ambient pressures were collected to compare with the model.

Finally, in the large study, four IPN spectrometers operated at 405, 532, 671, and 1047 nm, were used to characterize the optical properties of black carbon aggregate (BCAgg) and black carbon percolated aggregate (BCPAgg) particles. A scanning mobility particle sizer (SMPS), PTFE filter samples, and microanalysis particle sampler were also operated at the same time. The mass absorption cross-section (MAC) was calculated and compared for both BCAgg and BCPAgg particles.

2 Introduction and Assembly of an Integrated Photoacoustic-Nephelometer (IPN) with 1047 nm Laser

2.1 Introduction to Photoacoustic Nephelometry

The integrated photoacoustic-nephelometer (IPN) spectrometer is a widespread and practical tool for trace detection and characterization of all gases and particles[40]. It has been used for the balloon based studies of nitric oxide and water vapor detected in the stratosphere, and for sensitive measurements of trace gases and aerosols light.[32] Harren et al. discuss the history of photoacoustic technology can be traced back to 1880, when Alexander Graham Bell found thin discs exposed to a rapidly interrupted beam of sunlight could generate sound waves[16]. Aerosol light absorption measurements by photoacoustic instruments has been accomplished for more the more than 30 years.

2.1.1 Introduction to Photoacoustic Effect

Fig. 2.1 shows the principle of the photoacoustic effect for aerosols. Light pulses absorbed by the particle cause the temperature increase. Heat transfers by conduction from the particle to the surrounding air, creating a pressure disturbance or sound wave. Compared to the expansion of the surrounding air, the volumetric change of the particle is negligible. This transformation of light energy into sound is known as the photoacoustic effect. In the IPN spectrometer, the sound wave is measured by a microphone. Aerosol light absorption is quantified by use of a

calibrated laser power meter and a microphone. The particle temperature increase is less than 1 K for typical aerosol sizes and the laser power applied.
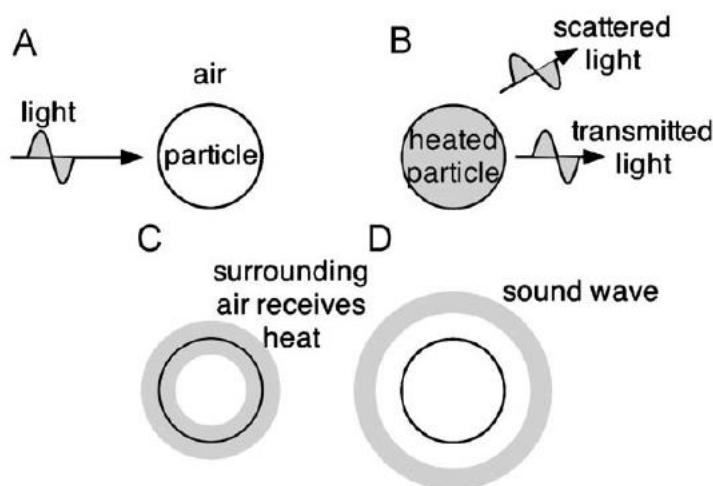
Figure 2.1 Principle of photoacoustic effect for aerosols

(A) Light is incident on a particle. (B)Some of the incident light is absorbed by the particle, some is transmitted, and some is scattered. The particle is heated by light absorption. (C)Heat transfers from the particle to the surrounding air. (D)The surrounding air expands upon receiving heat, resulting in an outgoing acoustic wave.

In the evaporation of semi-volatile compounds such as water vapor, the mass transfer from the heated particles to the ambient environment can also contribute to the acoustic pressure. Compared to heat transfer, mass transfer is less efficient because part of the laser energy is needed as latent heat to transform the liquid to vapor phase[41]. Particles need to be dried first to avoid ambiguity in distinguishing between heat and mass transfer, because water is the most common semi-volatile compound. Thus, quantifying light absorption of aerosols with a high percentage of liquid components is still an open question.

A small dry aerosol of radius r, illuminated by a laser of irradiance I, undergoes a temperature change $\Delta T(t)$ and volume expansion. The temperature change $\Delta T(t)$ at time t = 0 is given by Chan[42] as a function of time as:

$$\Delta T(t) = T_\infty \left[1 - \exp\left(\frac{-t}{\tau}\right)\right], \tag{2.1}$$

where the T_∞ is the final particle temperature and it is expressed as

$$T_\infty = \Delta T(t = \infty) = \frac{I Q_{abs} r}{4\kappa_a}, \tag{2.2}$$

Q_{abs} is the efficiency of light absorption, κ_a is the thermal conductivity of air, and τ is the characteristic time for the particle to heat up (or cool to ambient when the beam is turned off). τ is defined as

$$\tau = \frac{r^2 \rho_{particle} C_{p\_particle}}{3\kappa_a}, \tag{2.3}$$

where $\rho_{particle}$ is the particle mass density and $C_{p\_particle}$ is the particle heat capacity per unit mass. Thermal relaxation (i.e., the time it takes for heat to transfer out of a particle compared to the frequency ν used to modulate the laser beam power in continuous wave photoacoustics) reduct the photoacoustic signal by a factor of f, with

$$f = \frac{1}{1 - i2\pi\nu\tau} = |f| \exp(i\theta), \tag{2.4}$$

where θ is the phase shift between the light modulation and the resulting microphone signal.

Table 2.1 gives a series of signal reduction factors, f, for different aerosol diameters, d, for common parameters.

Table 2.1 Signal reduction factors, f, as function of particle diameter, d, for typical parameters

d (μm)	Q_{abs}	T_∞ (mK)	τ (s)	$\rightarrow f \rightarrow$	θ (deg)
0.01	0.0688	0.1	4.6×10^{-10}	1.00	0.0
0.1	0.844	13.1	4.6×10^{-8}	1.00	0.0
1	1.25	194	4.6×10^{-6}	1.00	2.5
2.5	1.03	400	2.9×10^{-5}	0.97	15
5	0.94	727	1.2×10^{-4}	0.68	47
10	0.88	1366	4.6×10^{-4}	0.22	77

2.1.2 Photoacoustic Resonator Design for Measuring Optical Properties of Aerosols

Cylindrical acoustic resonators have been widely employed for aerosol light absorption measurements applying the photoacoustic method. Radial, azimuthal, and longitudinal plane wave modes have been used. The radial mode is the fundamental breathing mode of a circular cross section resonator, and the plane wave mode has pressure fluctuations along the cylinder axis. The operating frequency and heat transfer from particles to the surrounding air during the acoustic cycle determine the maximum dimension of the resonator. The resonator design is a tradeoff between the practical need to allow the laser beam and sample to pass though the resonator and optimal acoustic pressure level for maximizing the instruments performance. Also, it is desirable to have continuous flow through the resonator. For the measurements by IPN systems, a signal only appears only when an absorber is detected. Microphones have a very large dynamic measurement range and thus provide ideal sensors for instruments.

2.1.3 Radial and Azimuthal Wave Resonator

Fig. 2.2 shows a schematic cross-section of the radial wave photoacoustic resonator. Aerosol flow enters and exits the resonator at pressure nodes while the laser beam passes though the

resonator. The microphone is located at the center of the wall. The radial mode is circularly symmetry about the center of the microphone. An early adaptation of radial resonators for trace gas detection proved the advantage of acoustic amplification of the acoustic standing wave amplitude[43]. This work was followed by an acoustic resonator design that makes use of a cylinder axis ratio facilitating Brewster's angle windows for operation of the acoustic cell within a laser cavity[44]. A comparison of radial and azimuthal mode cylindrical resonators indicated some practical signal advantages of the azimuthal mode resonator[45] using NO_2 as a calibration gas, though this finding may be due to differences in the acoustic background levels at the different operating frequencies used (around 2 kHz for the azimuthal mode, 4 kHz for the radial mode).
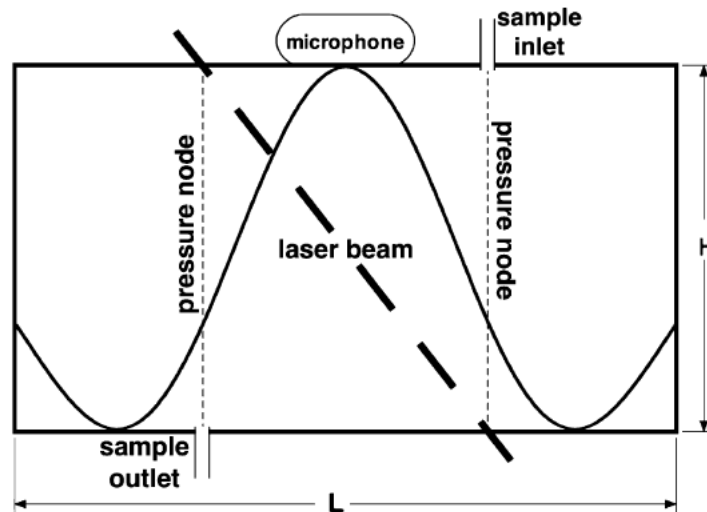
Figure 2.2 Schematic diagram of the radial wave photoacoustic resonator

2.1.4   ½ Wavelength Plane Wave Longitudinal Resonator

Fig. 2.3 shows a schematic cross section of the ½ wavelength longitudinal mode plane wave resonator. Pressure nodes are toned at the ends of the acoustic resonator. Larger buffer volumes

are applied in order to simulate a pressure release boundary condition. Buffer volumes would also detune noise from the inlet and from light absorption by aerosol deposited on the windows. The aerosol sample air flow is pulled continuously though the resonator with a fixed flow rate (0.7 – 1.4 Lpm).

A multipass resonator of this type has been developed for aerosol light extinction and absorption measurements[46]. This instrument has been thoroughly characterized with laboratory-generated aerosol and was recently used to identify a 40% bias for aerosol light absorption measurements by a commonly used filter-based method when a substantial fraction of the aerosol mass is organic carbon[47].
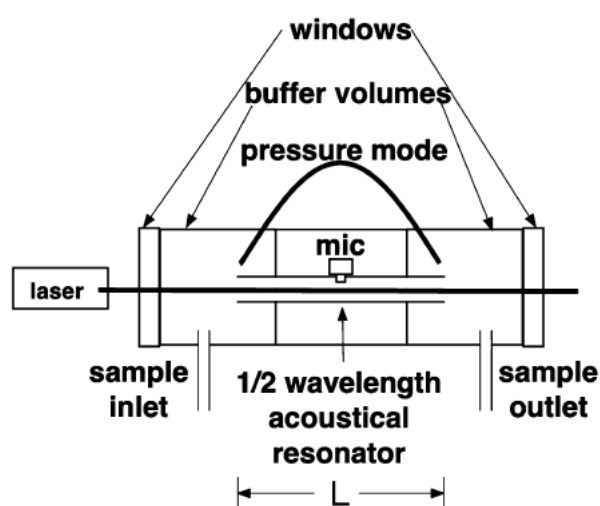
Figure 2.3 Schematic cross-section of the ½ wavelength longitudinal mode plane

2.1.5 Full Wavelength Plane Wave Longitudinal Resonators

The full wavelength plane wave longitudinal resonator, also known as a banana resonator was developed for trace gas detection[48]. A modified version was developed and employed for aerosol light absorption analyzation[49, 50]. The idea of the full wavelength plane wave longitudinal resonator was extended to the U-shaped resonator shown in Fig. 2.4, which has

been discussed in multiple publications[51, 52]. In a resonator, the aerosol light absorption is

defined as[49]

$$\beta_{abs} = \frac{p_m A_{res} \pi^2 v}{P_L(\gamma - 1)Q},$$ (2.5)

where p_m is the microphone pressure at the resonance frequency v, P_L is the Fourier

component of the laser power fluctuating at the same frequency, A_{res} is the resonator cross

section area, γ is the ratio of isobaric and isochoric specific heat, and Q is the resonator

quality factor. The accuracy of the equation for aerosol light absorption has been confirmed by

experiments using light absorbing calibration gases (such as NO_2)[18].

The full wavelength plan wave longitudinal resonator has been applied to measure aerosol light

absorption from ambient and sampling sources. Examples have been shown in Table 2.2

below:

Table 2.2 Examples of reported aerosol light absorption measurements using full wavelength
plane wave longitudinal resonator

Place	Source	Laser Wavelength (nm)
China	Particles from urban area	532
Amazon	Amazon Basin wildfires	532
South Texas and north central Oklahoma	Emissions from biomass burning	532
Two sites near Mexico City	Black carbon emission	870
Aloft above Monterey, California, and north central Oklahoma	Emissions from biomass burning and urban area	676
Near border between United States and Mexico	Black carbon from vehicles	1047
United States	Laboratory generated biomass burning emissions	405 and 870

Fig. 2.4 reveals some practical considerations necessary for quantitative photoacoustic spectroscopy. The microphone and piezoelectric transducers are located at pressure antinodes, the inlet and outlet ports are located at pressure nodes to allow for sample air and laser beams to enter and exit. To maintain the quality of the acoustic signal, a critical orifice is employed to set the flow rate and to send loud pump noise back downstream towards the pump instead of into the instrument. A pressure equilibration capillary maintains the condenser microphone at ambient pressure so that the microphone sensitivity is held constant even when the sample inlet is connected to a sampling plenum at pressure substantially lower than ambient. A scattering sensor in the middle part of the resonator provides reciprocal nephelometer measurements of aerosol light scattering[53], and blocks the low frequency sound outside the resonator. Detuning tubes act as band stop filters at the operating frequency to reflect unwanted sound from the coupling regions away from the main resonator region, especially coherent sounds created by light absorption of particles on the resonator window. The piezoelectric transducer is used periodically to determine the resonator resonance frequency and quality factor for use in Eq. (2.5), and to determine the peak acoustic pressure at resonance. Recently, a modified version microphone that includes both microphone and piezoelectric functions has been applied in resonator systems (such as our IPN). The production of sound by the photoacoustic method occurs in the horizontal part of the resonator section, where the laser beam overlaps with the sample air near, and at the pressure anti-node located at the center of this section.
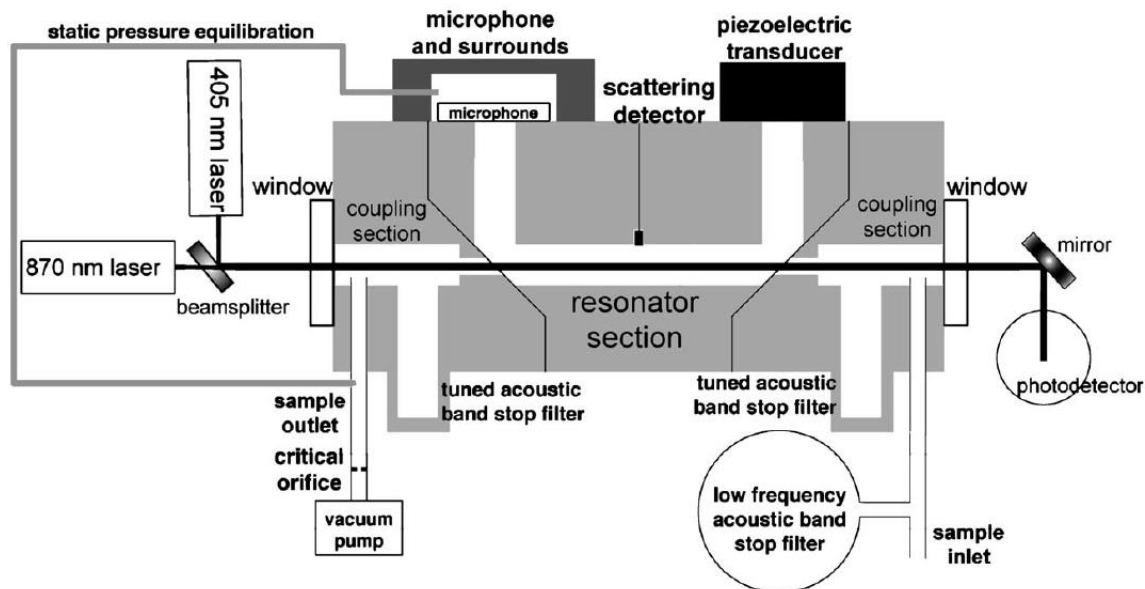
Figure 2.4 Schematic of a full wavelength plane wave longitudinal resonator

2.1.6 Nephelometer and Extinction-Minus-Scattering Techniques

One direct method to characterize the aerosol absorption coefficient is to measure both the aerosol extinction coefficient and scattering coefficient. The absorption coefficient can be calculated from the difference between the extinction and scattering coefficients. Ideally, both measurements are performed simultaneously and in the same sample volume to minimize systematic errors due to the inhomogeneous nature of the sample.

In 1979, H. E. Geber developed a 12 L portable cell with a 633 nm He-Ne laser[54]. The extinction coefficient measured by alternating measurements at $\approx$ 20 Hz of the laser power entering and exiting the multi-pass cell. The result was a transmittance measurement with a mean resolution of $\pm$0.16%, corresponding to an extinction resolution of $\approx \pm 10^{-4}$ m^{-1}, limited by the mechanical stability of the cell, which was onboard a Navy vessel at sea[54]. At the same time, the scattering coefficient was measured by a cosine sensor with a mean resolution of $\pm$5×10-6

m^{-1}. The instrument was calibrated by using filtered air, and the span of the reciprocal nephelometer was measured using Freon 12.

The next generation of extinction-minus-scattering instruments was developed by Weiss et al. at the University of Washington. It was a single-pass, $\approx$ 100 L volume extinction cell with a length of 2.4 m and the extinction resolution of $\approx$ 10^{-5} m^{-1} [55]. This cell was operated at a wavelength of 538 nm together with a three-wavelength nephelometer to measure the scattering coefficient. The absorption coefficient was obtained from intercomparison with those determined by an integrating plate technique[7]. Further work from Weiss et al. resulted in a computer-operated system based on a single-pass, 6.4 m extinction cell with a laser at 538 nm. The system was calibrated with a non-absorbing aerosol whose scattering coefficient was the same as its extinction coefficient[56]. A temperature-regulated reference detector was used to normalize the measured intensity to constant lamp brightness yielding a lower detection limit for the extinction coefficient of $\approx$ 2×10^{-5} m^{-1}. In another study, a three-wavelength nephelometer was used to measure the absorption coefficient of airborne aerosol from forest fires[57] and oil fires[58]. In 2005, Virkkela et al. reported a modified version of this instrument. Different from the older version, the system employed a dual-pass extinction with a 3.3 m sample volume resulting in a 6.6 m extinction path. The scattering coefficient was measured by a three-wavelength TSI nephelometer (model 3963, TSI, St. Paul, MN, USA) at 367, 530 and 660 nm. The extinction coefficient was calculated from the ratio of the signal and reference detectors after calibration with filtered air. An in-depth analysis of laboratory measurements yielded a detection limit (defined as three times the standard deviation of the noise) of 5×10-6 m^{-1}, and an accuracy (defined as the difference of extinction and scattering coefficient for

non-absorbing aerosols) of $\approx 10\%$ in the worst and $< 1\%$ in the best laboratory experiments[59].

This instrument was operated together with a TSI nephelometer (model 3963) for the absorption coefficient measurement. Measurements spelled out during the Reno Aerosol Optics Study (RAOS)[60] agreed in general to better than 10% with those data of a photoacoustic instrument[59, 60].

In 2005, Schnaiter et al. reported an extinction-minus-scattering system with a wider spectral range (190 to 1500 nm) and better spectral resolution (≈ 2 nm)[61]. A 7.6 L, 5 m dual-pass sample tube resulted in a 10 m extinction path. The sampling light source was a deuterium-halogen lamp, coupled to the sample tube with a UV-stabilized optical fiber. The transmitted light was coupled through fiber optics with an acceptance angle of ≈ 4 mrad to a two-channel diode array spectrometer. The second spectrometer channel was employed to monitor the emission of the lamp maintain the accuracy of measurements. A thermally insulating box was used to reduce thermal drift. The aerosol absorption coefficient was measured by a three-wavelength TSI nephelometer (model 3963). The SSA for soot and biomass burning was 0.2 and 0.74, which was in good agreement with photoacoustic[50] and other extinction-minus-scattering measurement techniques[60, 61].

The extinction-minus-scattering technique is a promising method to measure aerosol light absorption. However, the path length is limited, and thus so are the detection limited of the extinction coefficient measurements. As a result, extinction-minus-scattering technique instruments are commonly used to measure laboratory generated particles or near-source aerosol plumes in the ambient atmosphere with relative low SSA. The detection limit should be below 1 Mm^{-1} to ensure the accuracy of the instrument's measurement[62]. A different type of

extinction instrument, based on cavity ring-down (CRD) techniques, uses high quality optical cavities with highly reflecting mirrors (e.g., R = 99.995%) to realize effective optical path lengths of multiple kilometers in a compact (length < 1 m) cell. Such intruments have recently been used to measure aerosol extinction with detection limits well below 1 Mm^{-1} [63]. CRD instruments have been applied to measure a variety of aerosols, such as airborne aerosols[64], biomass burning[65], coating aerosols[66] and single particles[67, 68].

In order to avoid error during measurements, it is preferable to use the same sample volume for both scattering and extinction measurements. Newer Instruments combine aerosol CRD components and reciprocal nephelometers together in the same volume and laser beam[64]. In 2003, Strawa et al. developed an instrument that utilizes a CRD ring resonator and a diode laser at 690 nm[63]. The reciprocal nephelometer uses a detector with a diffuser to achieve a truncation angle of about 15°, about two times worse than the TSI nephelometer (model 3963). In 2008, to characterize individual particles, Sanford et al. use an external cavity cw diode laser operating at 672 nm frequency-locked to a CRD ring resonator together with a reciprocal nephelometer based on a unique spherical/ellipsoidal mirror pair with a truncation angle of 8.5°[69]. In addition, this instrument measure near-forward scattering (4.2° to 8.5°) within the near-forward truncation angle for particle sizing. This additional measurement might also be useful for further reducing or correcting truncation errors.

Although these CRD and nephelometer combination instruments increase the sensitivity of ambient aerosol light absorption and SSA measurements, in-depth testing and intercomparison with photoacoustic and other techniques still need to be completed. There are several sources of error in extinction-minus-scattering techniques: errors can be introduced when measuring

pure-scattering aerosols, due to the subtraction of near-identical values for extinction and scattering coefficients, and the influence of nephelometer errors can affect measurements of large particles[70]. Moreover, near-forward scattering corrections for finite acceptance angle extinction measurements have not been analyzed for the stable resonators used for CRD extinction measurements, and the use of separate instruments for extinction and scattering measurements can lead to errors. For hydroscopic particles at high relative humidities, potentially different sample temperatures can result in different relative humidities and consequently different particle sizes.

2.2   Instrumentation Design and Assembly

The design of IPN used in this work is modified from the design from Dr. William Patrick Arnott at the University of Nevada Reno[50]. In this project, we constructed an IPN operating at 1047 nm. Fig. 2.5 shows a schematic view of the IPN. The principle of operation is as follows. The laser is modulated at the acoustic resonance frequency of the IPN. The scattering detector and laser power meter convert laser power to acoustic pressure through aerosol expansion. A microphone measures the acoustic signal and converts it to absorption values. In this section, we will discuss the construction of the measurement system, laser alignment, component assembly, and calibration process.
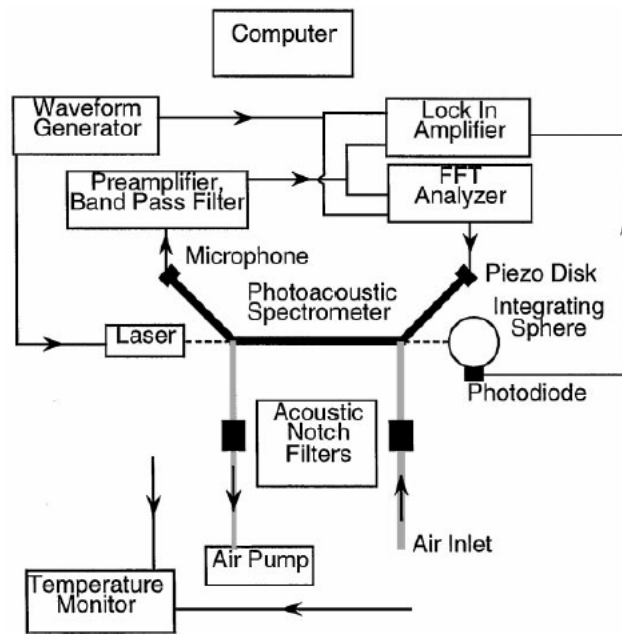
Figure 2.5 Block diagram of the Photoacoustic-Nephelometer (PA) system

2.2.1 Individual Parts of the IPN spectrometer

A resonator (Fig. 2.6) is commonly used to increase the acoustic pressure at the microphone. It is made of a cylindrical stainless steel acoustic cell with two notch filters, and two copper tubes as the inlet and the outlet for the aerosol flow, an aperture cell, and a window on each side of the acoustic cell. At the front side, two mirrors (with four tuning knobs to adjust the angle) reflect the laser illumination into the acoustic resonator. A laser power meter is attached at the end of the resonator to detect the laser power loss. The laser and resonator are fixed on a stainless steel board with two rubber damping absorption blocks on the bottom. Finally, the stainless steel board is fastened to the bottom of a steel box (Fig 2.7).
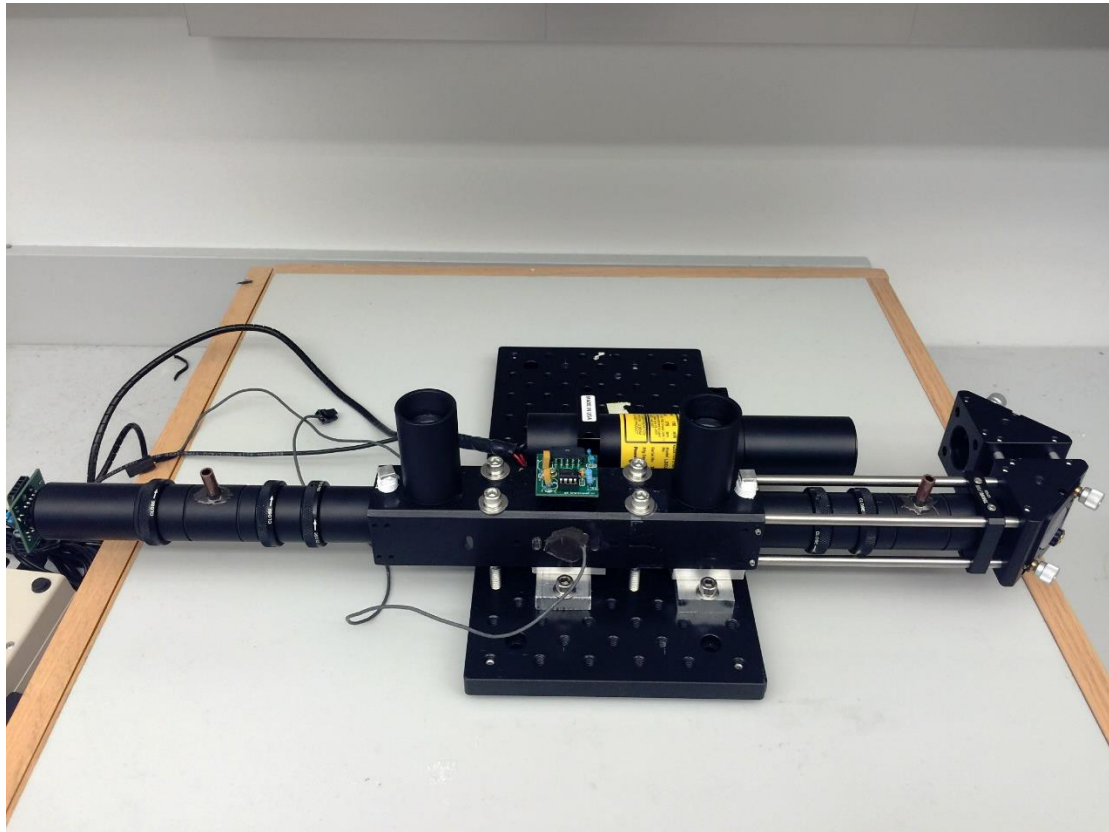
Figure 2.6 View of the acoustic resonator

Figure 2.7 View of the resonator installed in the enclosing (assembly) box.

Two Helmholtz resonators (Fig. 2.7) were placed at the aerosol inlet port on the steel box to absorb the noise out of the IPN, and it was connected with the aerosol inlet on the resonator with static dissipative silicone tubing. For the outlet port, a valve was installed to stabilize the flow rate in the system (0.7-1.3 lpm). After that was the RH and temperature sensor and a HEPA filter are inline with a tee adaptor with one side connected to the pressure broad and the other side attached to the outlet on the resonator.

The other components (Fig. 2.8, 9, 10, and 11) include a microphone board, power/relay board, USB DAQ, pressure board, power board, and breakout board, all fastened around the walls of steel box.
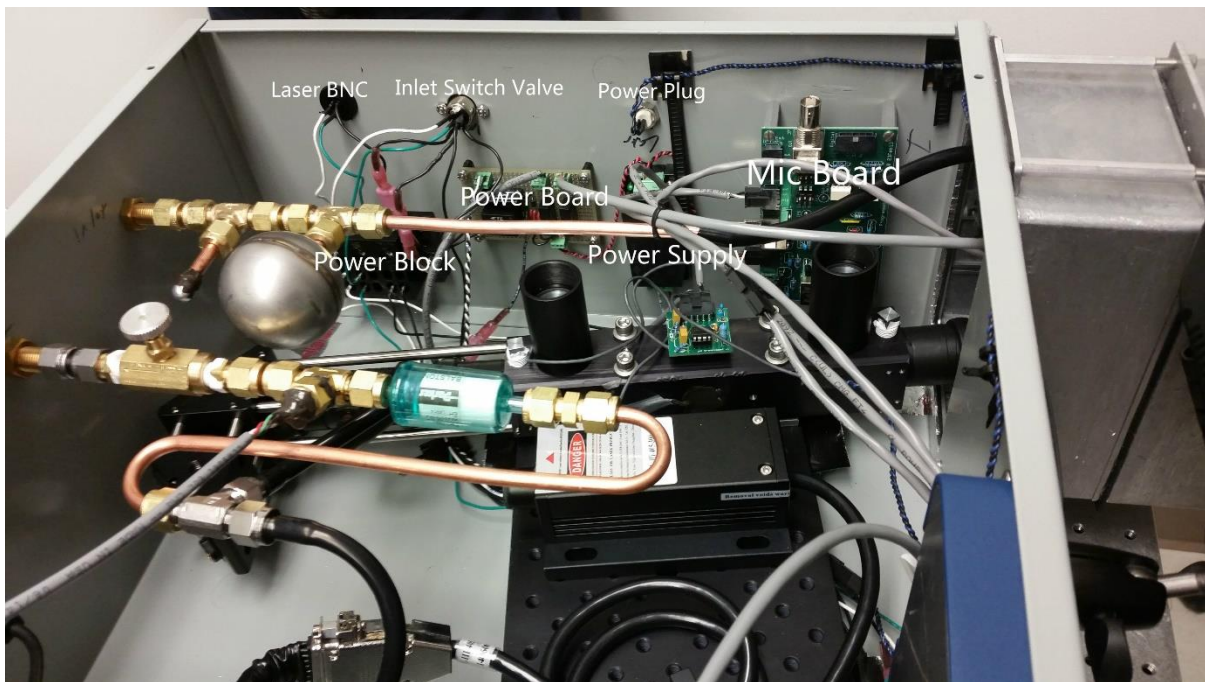
Figure 2.8 View of the resonator installed in the box- Horizontal Top View
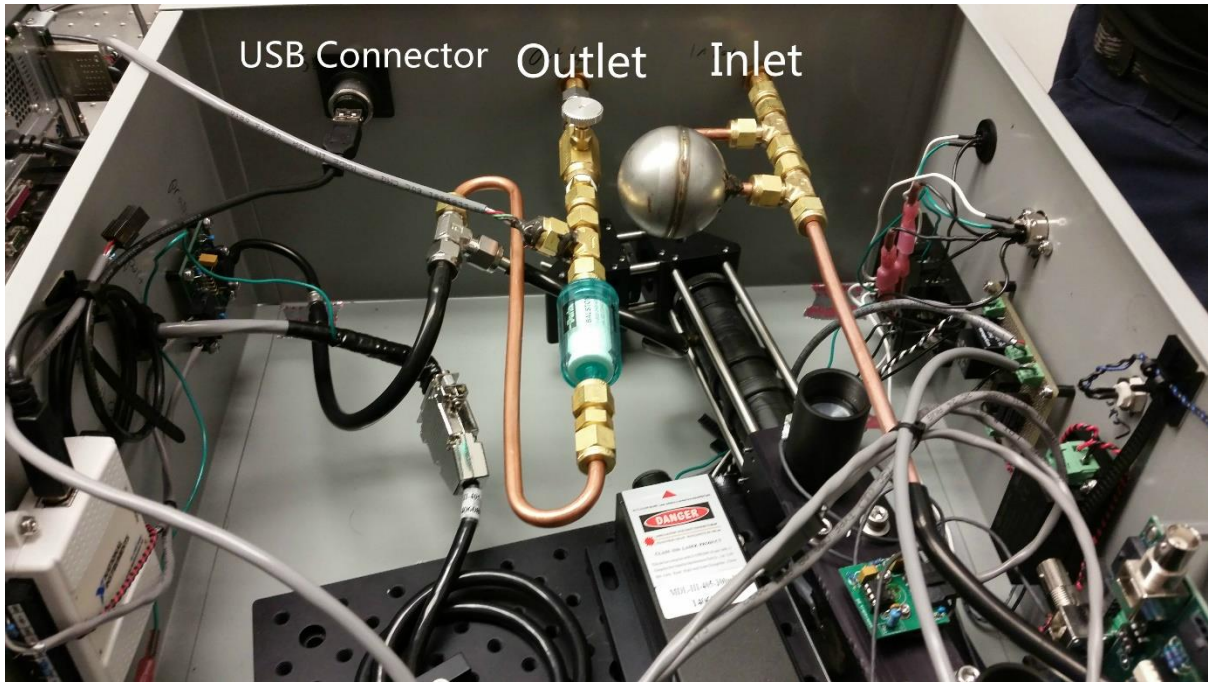
Figure 2.9 View of the resonator installed in the box- Parallel Top View
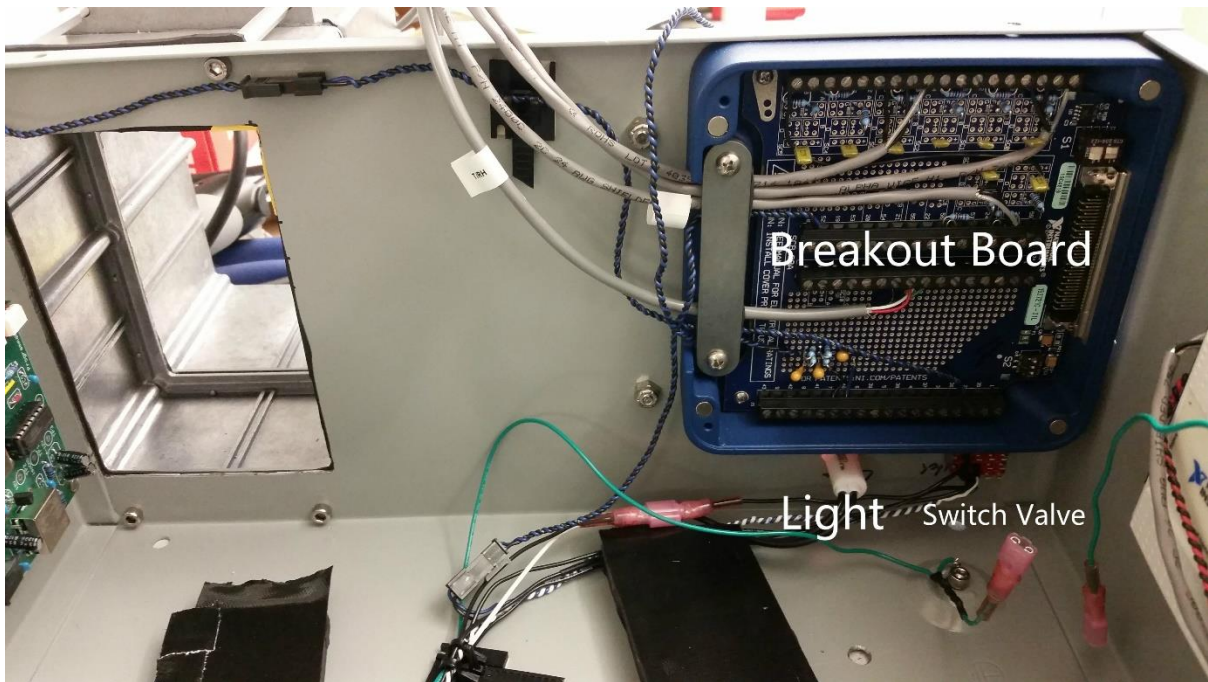
Figure 2.10 View of the resonator installed in the box
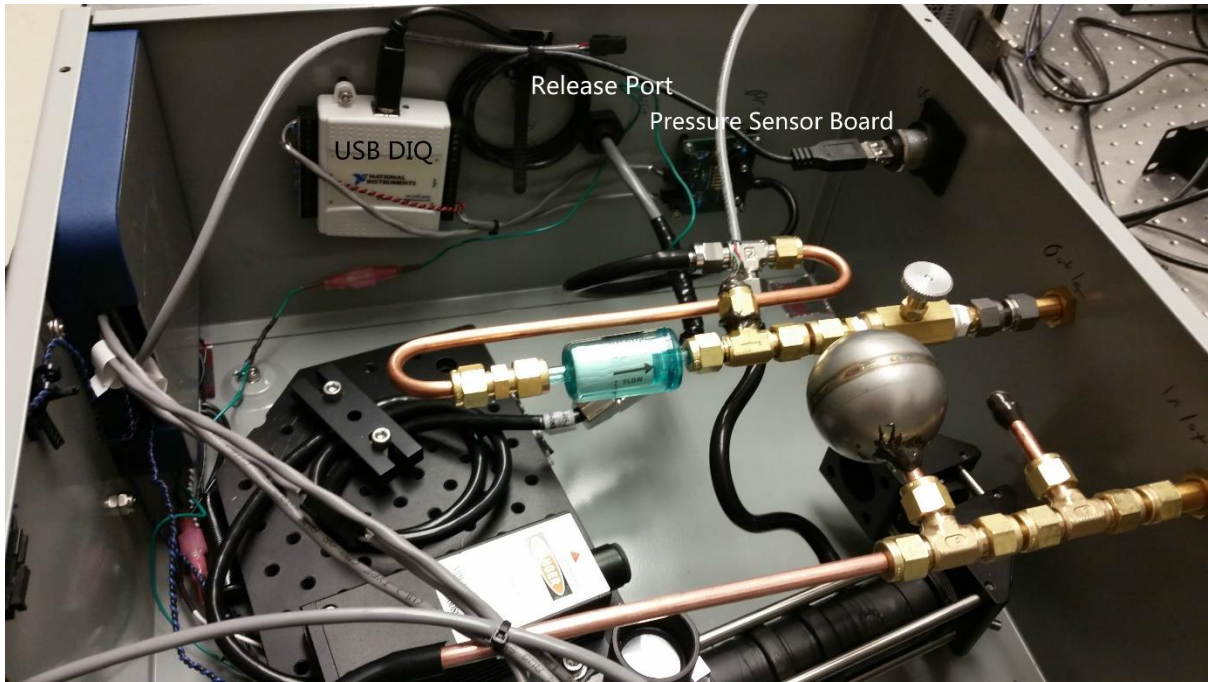
Figure 2.11 View of the resonator installed in the box- Side View

2.2.2 Laser Alignment

After the assembly of the components, careful alignment of laser and resonator is needed to ensure that the laser is not diffracted by the edges of the apertures in the resonator or reflected back to the scattering photodiode.

To begin the calibration, we replaced the laser power meter at the end of the resonator with a portable laser power detector. All the apertures were set to the largest opening. We then carefully turning the four knobs to adjust the angle of mirrors until the value of the laser power detector reached the maximum. Then we place a laser target at the end of the resonator, and adjusted the size of the apertures to concentrate the laser beam. We repeated the two steps above until the laser power reached a maximum and the spectrum is concentrated. Alignment was achieved when an acceptable balance is found between maximum laser power and minimum stray light detected by the scattering photodiode.

Once the instrument was aligned, the laser power meter was calibrated by measuring the raw voltage output of the detector as well as the laser power directly with a commercial laser power meter. A calibration factor in mW/V was derived and programmed into the instrument's LabVIEW program.

2.2.3   Assembly of the Components

As shown in Fig. 2.12, the instrument is well sealed against dust and moisture and is mounted in a road case designed for standard 19" rack equipment, along with the computer that operates the instrument, a HEPA filter and valve for self-calibration, the laser power source, and a line filter for clean power.

Figure 2.12 View of IPN packed in the rack

3   Instrument Calibration, Evaluation and Performance

3.1   Instrument Calibration

After assembling of the instrument, we calibrated the absorption and scattering measurement. Single scattering albedo (SSA), which is defined as the ratio of the scattering coefficient to extinction coefficient, is measured by the integrate photoacoustic-nephlometer (IPN) spectrometer. The sensitivity of the scattering coefficient measurement was initially examined using pure scattering aerosol (SSA close to 1) and comparing the measured scattering coefficient with the extinction coefficient calculated by the Beer-Lambert law. The sensitivity of the absorption coefficient was calibrated using strong light absorption aerosol (SSA close to 0) by comparing the obtained absorption coefficient with the difference of the extinction and scattering coefficients, which was already calibrated in the first step.

3.1.1   Introduction to Photoacoustic Calibration

The absorption and scattering calibrations are based on the measurement of single-pass light extinction. To measure the accuracy of β_{sca}, β_{abs}, and β_{ext}, the scattering calibrations are carried out using non-absorbing aerosols (salt). Absorbing aerosols (black carbon aggregate) are used for absorption calibrations. The calibration coefficients are determined by comparing the scattering signal (β_{sca}) and absorption signal (β_{abs}) to the extinction signal (β_{ext}). The relationship of these three parameters is given by

$$\beta_{ext} = \beta_{abs} + \beta_{sca}, \tag{3.1}$$

where βext is calculated by the Beer-Lambert law:

$$I = I_0 \exp(-\beta_{ext}L), \tag{3.2}$$

and I is the laser output strength measured by the photodiode at the end of the resonator, and I_0 is the initial laser power, which is found by testing. L is the length of the cell.

The calibration correction factor for the scattering coefficient may depend on the particle size because of the truncation error. Moreover, no reference has derived the relationship of the scattering correction factor as a function of particle size for IPN spectrometers, so we did not consider the influence of particle size on the scattering calibration in this study. Also, although the long-term stability of calibration correction factors and environmental parameter variations may affect the correction factors, these conditions are not discussed in this project.

3.1.2   Experimental Setup

Salt particles were used to calibrate the scattering coefficient. Fig. 3.1 is the experimental set up of the scattering calibration. Salt vapor was generated by a humidifier that sonicated salt solution. The salt vapor was dried by a diffusion dryer (Fig. 3.2). A control system was used to monitor the concentration of aerosol analyzed by the IPN spectrometers: a triangular control system (Fig. 3.3) with two pathways was used to monitor the consentration of aerosol. In the first pathway, a ball valve controlled the coneentration. The second pathway consisted a HEPA fiter and a second ball valve, which always open.
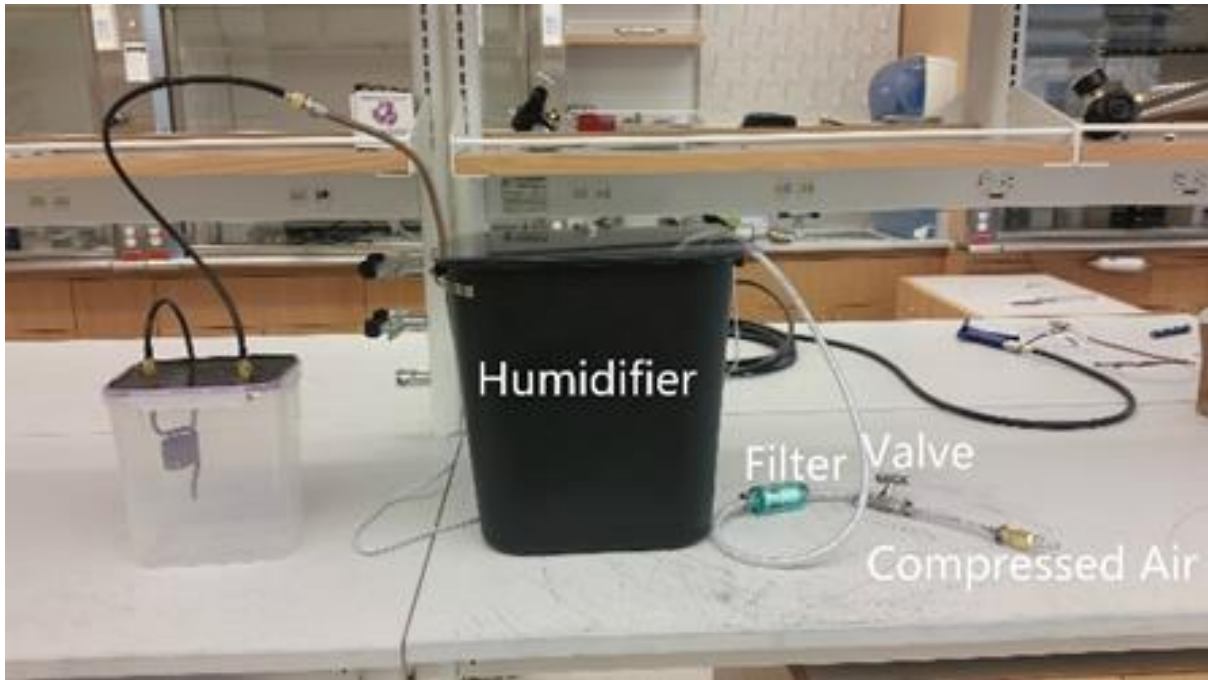
Figure 3.1 Experimental setup for scattering calibration (using salt particles)

Figure 3.2 Diffusion drier
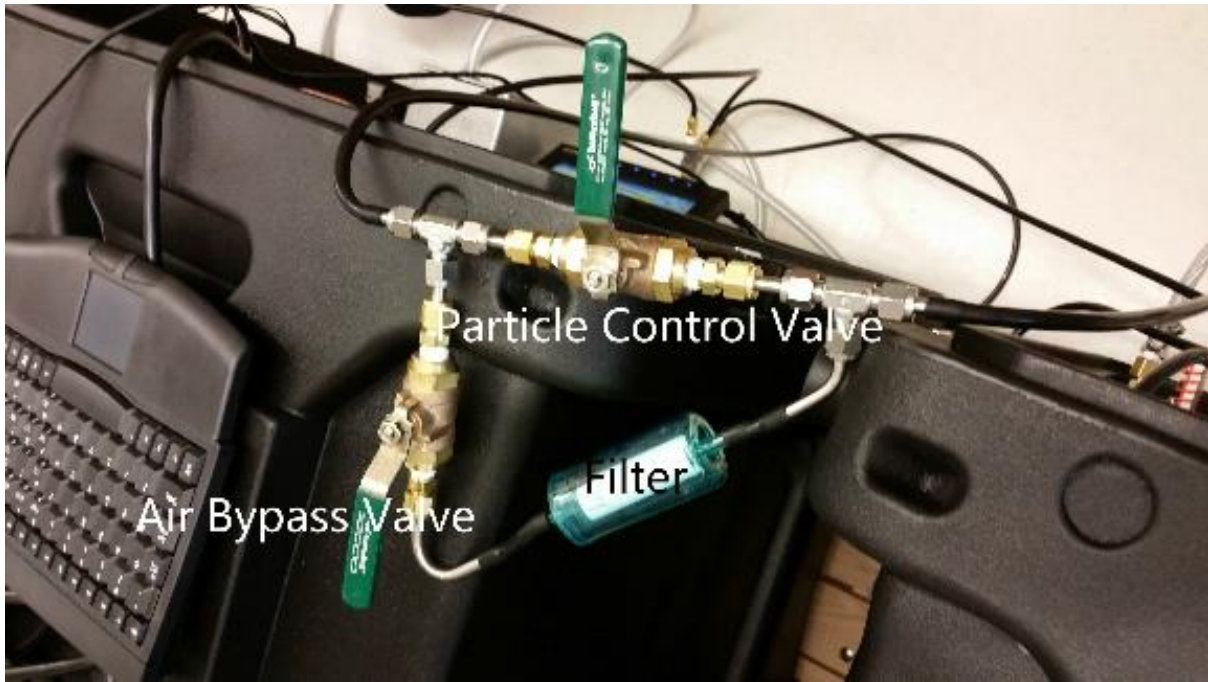
Figure 3.3 The triangular particle control setup

For absorption coefficient calibration, soot particles generated by a kerosene lamp were used.

Fig. 3.4 shows black carbon aggregate particles were generated by the kerosene lamp and then

dried by a diffusion dryer. During the generation of soot particles, a large quantity of NO_x is

also generated, which absorbs strongly at short wavelengths (375 and 405 nm). The absorption

by NO_x would affect the absorption coefficient measurement. In order to minimize this

influence, a dilution barrel was used to collect and mix the black carbon aggregate particles

from the diffusion drier. The dilution barrel was first filled with soot and NO_x, and then allowed

to sit for 10-15 mins to let NO_x settle to the bottom of the drum (the molecular weight of NO_x is

heavier than air), then the soot particles are pumped from the top of the drum to the measuring

instruments. The triangular control system described above was used to control the

concentration of soot aerosols analyzed by the IPN spectrometers.

Figure 3.4 The black carbon sub-micron aggregate generator

3.1.3   Calibration Process

The calibration of scattering and absorption measurements relies on the relationship between β_{abs}, β_{sca}, and β_{ext}. Because β_{ext} is equal to the sum of β_{abs} and β_{sca}, we expect that the β_{sca} of purely scattering aerosol (salt) is equal to its β_{ext} (measured by the laser power meter and calculated using equation (3.2)). By controling the concentration of salt particles, a variety of β_{sca} data could be collected. Then calibration software plotted the β_{sca} as a function of β_{ext} (Fig. 3.5), and the slope was taken as the calibration factor of the scattering measurement to calculate the new correction factor, using the formula below:
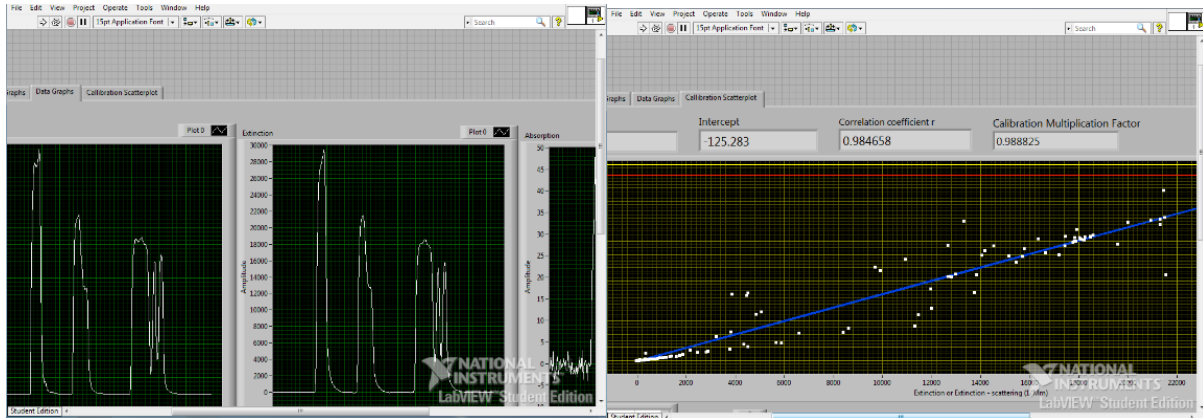
Figure 3.5 Calibration software screenshots and example of calibration result

$$New\ Scattering\ (absorption)Factor = Old\ Scattering(absorption)\ Factor *$$

$$Calibration\ Factor \qquad\qquad\qquad\qquad\qquad\qquad (3.3)$$

After saving the new correction factor was saved in LabVIEW software (Fig. 3.6), the IPN spectrometer needed about 10 mins to stabilize. After that, we repeated all steps until the calibration factor was close to 1, usually, we stopped at 0.95.
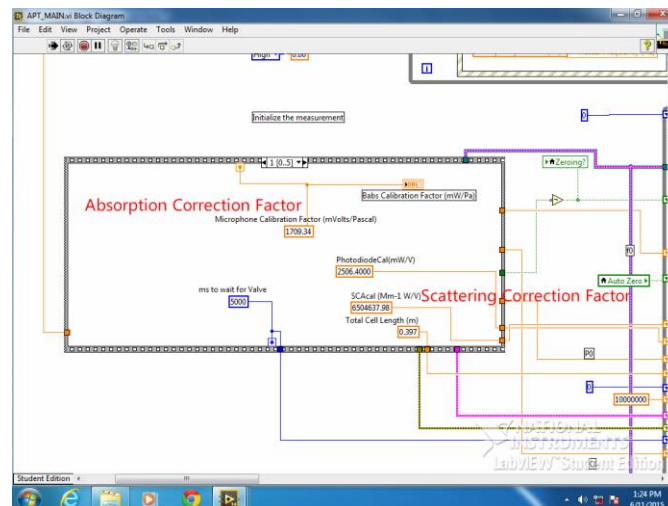
Figure 3.6 The correction factors in our custom-made PA LabVIEW program

Similarly, we expect the same 1:1 relationship between β_{abs} and β_{ext} using pure absorption aerosol (soot). The calibration factor for absorption is derived in the same way as for scattering. However, for the 375nm and 405nm IPN spectrometers, it is hard to increase the absorption calibration factor over 0.90 because the effects of NO_x.

3.1.4 Measuring Stability using Allan Deviation

The measurement resolution of IPN spectrometers is limited by similar random fluctuations of the measured quantity, which creat noise. At the same time, IPN experience some degree of variation with time, which is known as drift. Both noise and drift affect the signal value and limit measurement accuracy. In order to better understand the instrument's performance, noise and drift must be considered, which requires determining of frequency dependence of the noise and drift components during the measurement.

The most commonly used method is standard deviation: a low standard deviation indicates that the data tend to be close to the mean value, while a high standard deviation means the data tend to spread out over a larger range of values. However, standard deviation cannot distinguish noise or drift types. In contrast, Allan deviation analysis is a useful tool for evaluating the stability and precision of measurement signals.[71] In the plot of Allan Deviation, different types of noise and drift can be identified in the different plot regimes by their slope.[72] Here we explain and illustrate the methods of Allan Deviation and Overlapping Allan Deviation.

3.1.5 Allan Variance and Allan Deviation

The Allan variance is a two-sample variance formed by the average of the squared differences between successive values of a regularly measured quantity taken over sampling periods from the measuring interval up to half the maximum measurement time (Allan 1987).[73] The Allan deviation is defined as the square root of the Allan variance. Similar to the standard deviation, Allan deviation measures partial frequency fluctuations, but has the advantage of being convergent for most types of noise.

The original Allan variance is a time domain measure of frequency stability, which is defined as:

$$\sigma_A^2(\tau) = \frac{1}{(M-1)} \sum_{i=1}^{M-1} [y_{i+1} - y_i]^2, \tag{3.4}$$

where y_i is the ith of M fractional frequency values averaged over the sampling time interval τ.

If phase data are used, the Allan Variance becomes:

$$\sigma_A^2(\tau) = \frac{1}{2(M-1)\tau^2} \sum_{i=1}^{N-2} [x_{i+2} - 2x_{i+1} + x_i]^2, \tag{3.5}$$

where x_i is the ith sample of the N = M+1 phase value while τ is the measurement time interval.

The Allan deviation is, like the standard deviation, the square root of the variance

$$\sigma_A(\tau) = \sqrt{\frac{1}{(M-1)} \sum_{i=1}^{M-1} [y_{i+1} - y_i]^2}, \tag{3.6}$$

or, for phase data,

$$\sigma_A(\tau) = \sqrt{\frac{1}{2(M-1)\tau^2} \sum_{i=1}^{N-2} [x_{i+2} - 2x_{i+1} + x_i]^2}, \qquad (3.7)$$

Compared to ordinary deviation, Allan deviation can characterize a variety of noise types and convert them to a value that only depends on the number of samples.

3.1.6   Overlapping Samples and Overlapping Allan Deviation

Overlapping samples can be used to calculate the signal stability: the analysis is accomplished by utilizing all possible combinations of the data set[74]. As shown in Fig. 3.7, the overlapping samples method includes all possible pairs in the time period. The result has less statistical uncertainly and provides a better signal/noise ratio, but requires a longer computational time.
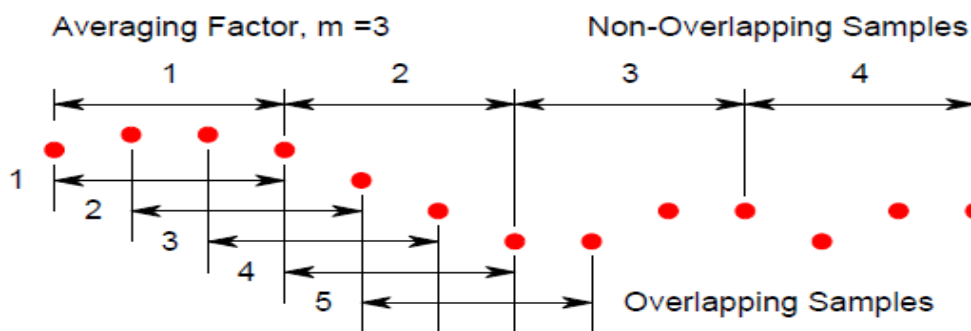
Figure 3.7 Example of overlapping samples

Overlapping Allan deviation is a form of the Allan deviation, $\sigma_A(\tau)$, which makes maximum use of a data set by forming all possible overlapping samples time interval τ. It can be determined from a series of M frequency measurements for averaging time $\tau = m\tau_0$, where m is the averaging factor and τ_0 is the measurement time interval. The formula

$$\sigma_A(\tau) = \sqrt{\frac{1}{2m^2(M-2m+1)} \sum_{i=1}^{M-2m+1} \left\{ \sum_{i=1}^{j+m-1} [y_{i+m} - y_i] \right\}^2}.$$ (3.8)

This expression is rarely used for large data sets because it is computationally intense. For phase data, the overlapping Allan deviation can be estimated as:

$$\sigma_A(\tau) = \sqrt{\frac{1}{2(N-2m)\tau^2} \sum_{i=1}^{N-2m} [x_{i+2m} - 2x_{i+m} + x_i]^2},$$ (3.9)

where N (N= M+1) is the number of measurements. The confidence interval of an overlapping Allan deviation estimate is better than that of a normal Allan deviation estimation because, even though the additional overlapping differences are not all statistically independent, they nevertheless increase the number of degrees of freedom and thus improve the confidence in the estimation.

3.1.7 Operation and Data Analysis

In our experiments, noise and drifts were studied by operating the IPN spectrometers with filtered air for 8 hours. Thirteen sets of data (104 hours in total) were collected for stability and detection limit analysis. An IPN spectrometer is considered to be stable over a length of time when the signal is free of drift. Averaging the signal over this period would reduce the influence of noise and hence the minimum detection limit of the instrument. For a signal which includes noise and drift, the overlapping Allan deviation is a helpful analytic tool.

We modified the MATLAB code provided by Fabian Czerwinski to calculate the overlapping Allan deviation for the absorption coefficient, scattering coefficient, and laser power signal at λ = 375, 405, 532, 671, and 1047 nm[42, 75]. The averaging time interval for all signals is 60 s, and

we abandoned data collected during instrument is auto-zeroing process, because the valve which switch the flow path to zeroing mode, introduced substantial signal deviations.

For a signal which includes random noise and instrumental drift, the Allan deviation first decreases proportionally with the reciprocal of the square root of the averaging time and then increases as instrumental drift becomes significant. From Fig. 3.8, the Allan deviation for absorption signal at all five wavelengths reach the peak between 0 to 2000 s and then remained stable in a certain range which did not increase significantly. A similar trend has been observed in scattering signal, unlike the findings of Uchiyama et al. and Shamar et al.[76, 77]. The stable trend after decreasing indicated that our instruments could be considered free of drift after a long warm up. But for laser power signal, epically for 671 nm laser, overlapping Allan deviation increased significantly after the curve reach the lowest, which means 671 nm laser cannot keep stable after a long time operation. Thus, 671nm IPN spectrometer need zeroing more often than other instruments when it is used for experimental measurement.
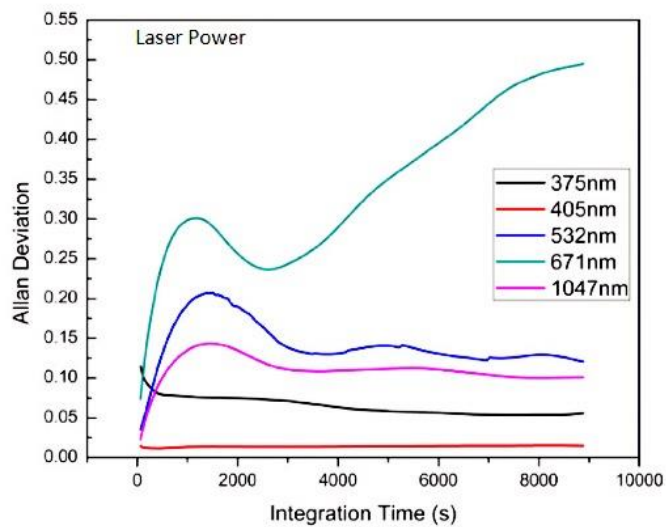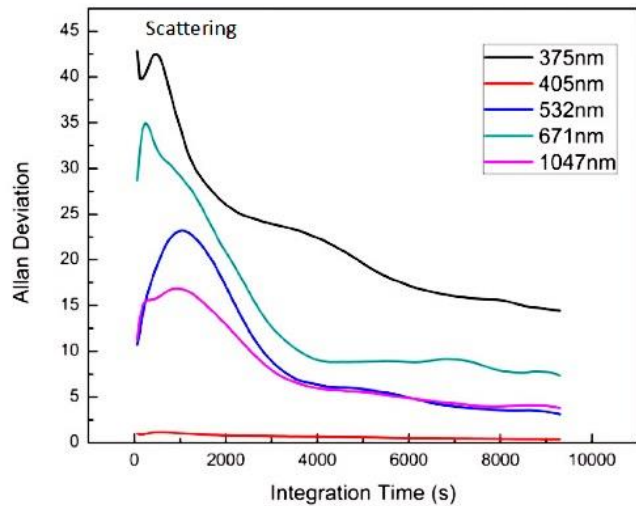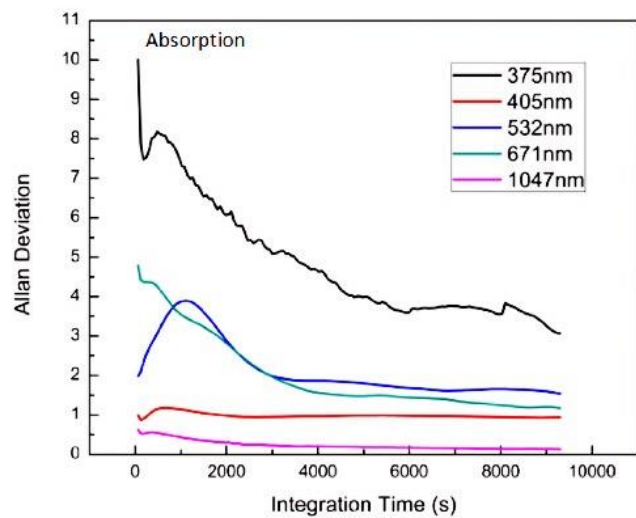
Figure 3.8 Overlapping Allan deviation plot

3.1.8   Results and Discussion

The typical Allan deviations (σ_A) for β_{abs} (and β_{sca}) at λ = 375, 405, 532, 671, and 1047 nm were estimated to be 2.60 (13.87), 0.98 (0.44), 1.35 (1.46), 1.18 (7.65) and 0.14 (3.42) Mm^{-1}, respectively. Uchiyama et al. perfomed Allan deviation analysis for β_{abs} (and β_{sca}), based on a photoacoustic extinctiometer (PAX) at λ = 375 nm and a three-wavelength photoacoustic soot spectrometer (PASS-3) at λ = 405, 532, and 781 nm for a 60 second integration time. Their reported values for the PAX were 0.82(0.81). The PASS-3 values for β_{abs} (and β_{sca}) were 0.55(0.15), 1.20(0.18) and 0.71(0.61) Mm^{-1}, respectively[76]. Sharma et al. reported a multi-wavelength photoacoustic-nephelometer spectrometer (SC-PNS), and the Allan deviation for β_{abs} (and β_{sca}) at λ = 405, 532, and 781 nm to be 0.4 (0.2), 8 (1.7), and 0.3 (0.8) Mm^{-1}, respectively[77].

In our study, the Allan deviations for β_{abs} at 405 nm and 532 nm were in good agreement with the data provided by Uchiyama et al., but the β_{abs} at 532nm was smaller by a factor of 6-8 compared to data from Shamar et al.. At 375 nm, the Allan deviation for our PA was 3 times larger than the result reported by Uchiyama et al.. The Allan deviations for β_{sca} at 375, 405 and 532 nm determined from our systems are all greater than those reported by Uchiyama et al. and Shamar et al., while β_{sca} (375nm), β_{sca} (405nm) and β_{sca} (532nm) were larger by factors of 17, 3, and 9 respectively[77]. There is no reference to evaluate IPN spectrometers with laser at 1047 nm or 671 nm using Allan deviation, so we do not have any data to compare.

3.2 Detection Limit

The minimum in the Allan plot indicates the optimum integration time. However, in the present study, it is difficult to observe a minimum point in all the Allan plots, so, following Uchiyama et al., we set the optimum integration time to 600 s for all signals to calculate the absorption and scattering detection limit for all IPN spectrometers. In the current study, the IPN spectrometers were set up to automatically zero the signal every 5 min to minimize the effect of signal drift. Using the same data that was used for Allan deviation study, Fig. 3.9 presents histograms for 104 h data by applying total 28 bins to each signal. For both β_{abs} and β_{sca} at all wavelengths, roughly Gaussian distributions are observed. The 2σ value for each distribution is considered to be the detection limit for 10 min averaged absorption and scattering measurements. At $\lambda = 375$, 405, 532, 671 and 1047 nm, β_{abs} (β_{sca}) were estimated to be 23.59 (102.32), 4.67 (3.38), 16.86 (65.93), 8.84 (72.29) and 1.15 (40.14) Mm^{-1}, respectively.

Percentage

Absorption Coefficient   Scattering Coefficient
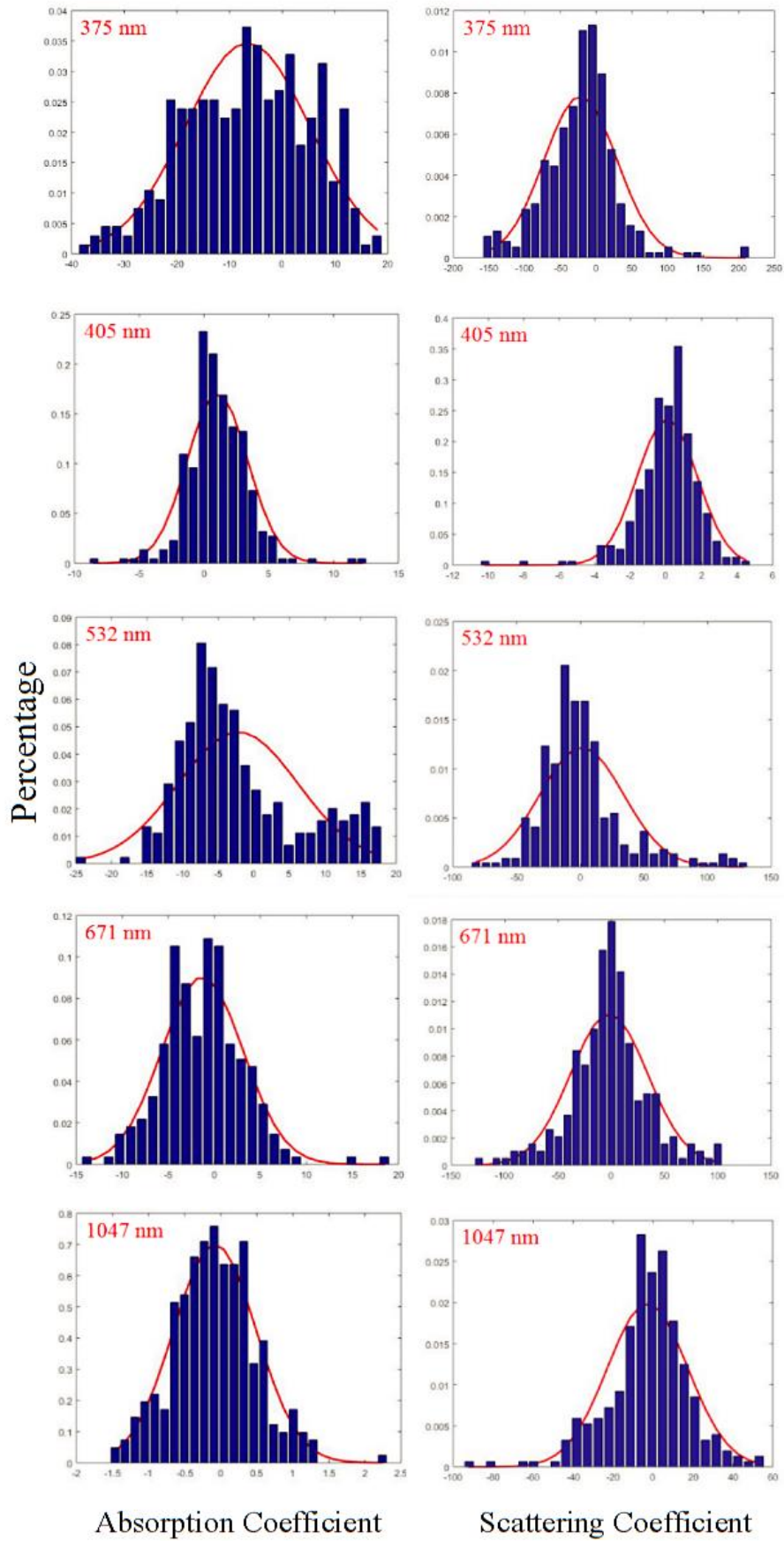
Figure 3.9 Histograms for 104 h data by applying total 28 bins for both βabs and βsca at all

wavelengths

3.3 Assessment of 1047 nm IPN Measurements in Airctafts: Pressure Sensitivity Analysis and Model Fitting

3.3.1 Considerations of Photoacoustic Aloft: Model Description

Photoacoustic-Nephelometer has been used both in source and ambient sampling of light absorbing aerosol. The absorption coefficient of PA is obtained from

$$\beta_{abs} = \frac{P_{mic}}{P_{laser}} \frac{A_{res}}{\gamma(\mathrm{RH}) - 1} \frac{\pi^2 f_0(T, P, RH)}{Q(T, P, RH)} = \frac{P_{mic}}{P_{mic}} \frac{A_{res}}{\gamma - 1} \frac{\pi^2 f_0}{Q}, \qquad (3.10)$$

where P_{mic} is the microphone pressure, P_{laser} is the laser power, A_{res} is the cross-sectional area of the resonator, γ is the ratio of isobaric to isochoric specific heats, f_0 is the resonance frequency, and Q is the quality factor of the resonator. The first form of equation (3.10) indicates the explicit dependencies on pressure, temperature, and RH. Relative humidity, temperature, and pressure are measured downstream of the photoacoustic resonator.

Equation (3.11) indicates that several parameters are a function of relative humidity (RH), temperature and pressure. To consider these parameters further, we first define the fraction of water vapor molecules as h, given by

$$\mathrm{h} = 0.01 \mathrm{RH}(\%) \frac{e(T)}{P}, \qquad (3.11)$$

where the saturation vaper pressure of water vapor at temperature T is

$$e(T) = 6.11(mb) \exp\left[\frac{a(T - T_0)}{T - b}\right], \tag{3.12}$$

where $a = 17.269, b = 35.860$, and $T_0 = 273.15$ for T > 273.15 K. The value of γ for moist air is

$$\gamma = \frac{7 + h}{5 + h}. \tag{3.13}$$

The variation of γ with air pressure and relative humidity in equation (2.15) is generally negligible, though of course one could easily take it into account since the requisite measurements to obtain it are available.

The speed of sound in the moist air is

$$c = \sqrt{\gamma \frac{1000RT}{29 - h}}, \tag{3.14}$$

where R is the universal gas constant and MKSA units are used[78]. The denominator of equation (2.19) is the average molecular weight of moist air, and equation (2.18) arises from the water vapor molecules having one more degree of rotational freedom than the main diatomic

constituents of air. The density of moist air, ρ, is

$$\rho = \frac{P(mb)}{RT}(2.9 - 1.1h). \tag{3.15}$$

The resonator quality factor can be expressed as

$$\frac{1}{Q} = \frac{Acoustic\ Power\ Cycle}{Energy\ Stored} = \frac{1}{Q_{transport}} + \frac{1}{Q_{loss}}, \tag{3.16}$$

where Q_{loss} is other fractional losses which include microphone signal fluxing due to its compliance, bulk acoustic losses in the gas mixture, and other fluid dynamical motions of the gas, such as vortex section generation where the resonator takes a perpendicular corner[60].

$Q_{transport}$, the resonator quality factor associated with transport losses of thermal conduction

and viscosity, is expressed as

$$Q_{transport} = \sqrt{\frac{\pi f_0 P(mb)(2.9 - 1.1h)}{RT\eta}} \, r \, \frac{\sqrt{N_{pr}}}{\sqrt{N_{pr}} + \gamma - 1}, \tag{3.17}$$

where the resonator radius (r) equals 1.3 cm, and η is the velocity of the moist air. N_{pr} is

the Prandtl number, expressed as

$$N_{pr} = \frac{\eta c_p}{\kappa}, \tag{3.18}$$

where κ is the thermal conductivity and c_p is the isobaric heat capacity per unit mass. The

Prandtl number of dry air at standard conditions is near 0.7.

The resonator is operated in an acoutic mode so that one full acoustic wavelength is spanned

by the resonator length L = 5.76 cm. This approach assumes that at the resonator ends, the

acoustic velocity goes to zero. However, because of dissipation of acoustic potential energy at

the resonator terminations in thermal boundary layers at the microphone, this boundary

condition is only approximate. This effect is small for the resonator discussed here. The

resonance frequency can be expressed in terms of the sound speed, quality factor, and

resonator length as

$$f_0 = \frac{c}{L}\left[1 - \frac{1}{2Q_{transport}}\right]. \tag{3.19}$$

Assuming the frequency shift is due entirely to wall absorption, and acoustic resonator would

provide a frequency (f_0) equals to c/L.

Equations (3.18) and (3.19) show that the primary variations of the resonator quality factor

and resonance frequency scale as the square root of the ambient pressure,

$$Q \propto \sqrt{P}. \tag{3.20}$$

The temperature for the measurement is actually the instrument temperature rather than the ambient temperature of the outside air, so temperature variations are less of an issue than pressure variations. Relative humidity changes will have a secondary effect on these resonator parameters when the local environment is heated.

Another important component of the photoacoustic absorption signal model is pressure. More specifically, pressure is related to the peak pressure at resonance (p_0), and it is given by

$$p_0 = \frac{\rho c v_0}{\pi} Q. \tag{3.21}$$

The acoustical resonator is periodically calibrated for determination of Q and resonance frequency by a piezoelectric transducer (already assembled as a component of the microphone in our IPN spectrometers). The microphone pressure is a function of the piezoelectric transducer velocity (v_0).

3.3.2   Data Collection and Model Fitting for 1047nm IPN

Combining equations (3.16) and (3.20) yields a model that shows the dependence of the quality factor on ambient pressure. Fig 3.10 shows measurements and the model fit for simulated measurements made abroad on aircraft, accomplished by using a needle valve at the instrument inlet to reduce the pressure inside instrument when the sample pump was operated. This model fits the measurements quite well at higher pressures (> 700 mb), and could be used to verify measurements aloft. But when the pressure is lower than 700 mb, the data and model deviate by up to 20%.
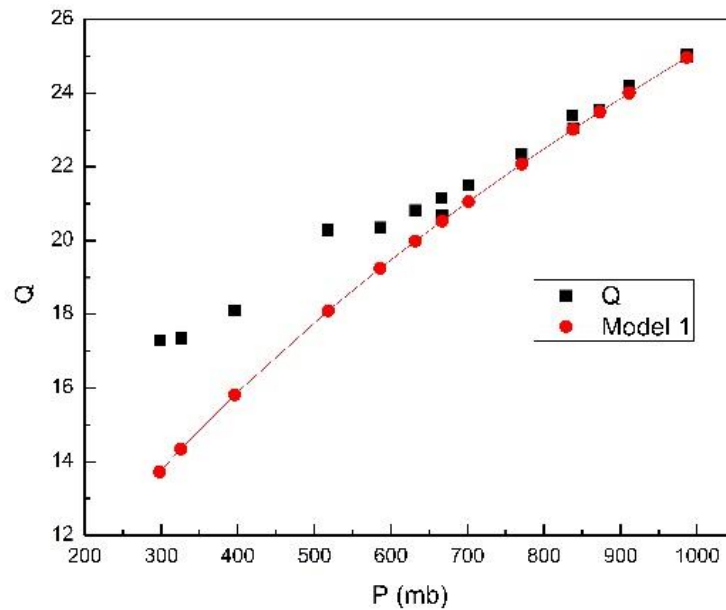
Figure 3.10 Resonator quality factor as a function of the ambient pressure, obtained with a valve on the inlet to simulate flight conditions

Fig. 3.11 shows a comparison of measurements of the peak acoustic pressure at resonance compared with model results from equation (3.21), as a function of ambient pressure in the range from 300 mb to 1000 mb as before. The linear behavior of the measured peak acoustic acoustic pressure in the range from 23 to 20 mb shows that the microphone calibration does not vary with ambient pressure, so light absorption measurements made aloft with the microphone will be accurate. But when the peak acoustic pressue is smaller than 20 mb, the collected data presents deviates from the value caculated from the model, which also shows that the method used for the microphone static pressure equilibration works well at lower pressure.
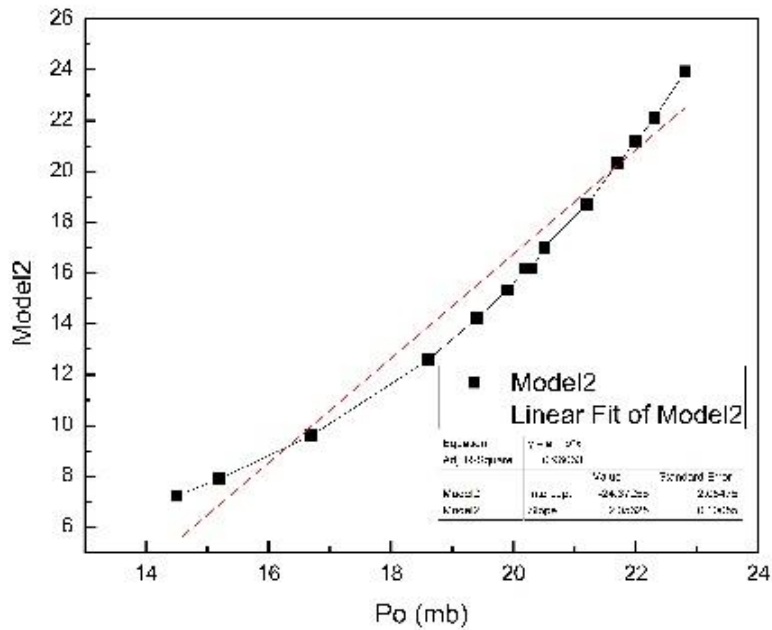
Figure 3.11 Comparison of measurements of the peak acoustic pressure at resonance compared with model

3.3.3 Conclusion

In summary, the acoustic performance of the 1047 nm IPN is adequate and characterized well enough for accurate measurements of the aerosol light absorption coefficient in aircrafts provided ambient pressue is higher than 700 mb. At lower pressures, the measuring data produced by 1047 nm IPN starts to deviate. This study has not taken into acount humidity, vibration, and ambient noise, which might also affect the accurcy of the IPN signals. Further study should be conducted to calculate the correction factor for airborne measurements at lower ambient pressure.

3.4   Instrument Performance

3.4.1   Experimentalal Set-up for Black Carbon Aggregate (BCAgg)
Measurements

The experimental set-up for Black Carbon Aggregate (BCAgg) characterization is shown in Fig. 3.12. BCAgg were generated by incomplete combustion of kerosene in a laminar diffusion burner and pumped through static dissipative silicone tubing to a 55-gallon stainless steel dilution barrel, where the particles tended to remain at the top while NO_x settled to the bottom. Particles for characterization were draw from the upper layer of the barrel's contents. Because the laser power of the IPN spectrometer takes hours to stabilize, the IPN spectrometer were turned on the night before any experimentation. At the same time, pump 2 was turned on and drew in air at 1.5 Lpm through the input ports of the IPN spectrometers. Hours later, when the lasers showed stable outputs, we turned on the burner and allowed the flame to visibly stabilize. Then we connected the IPN spectrometers to the barrel with pump 1 still running. Next we turned on pump 1 and let it run at 10.5 Lpm for 20 minutes. At that time, we turned off pump 1 and disconnected the sub-micron aggregate generator from the barrel. The IPN spectrometers continued to draw samples from the barrel.

The mass flow rate was measured by a 47 mm diameter in-line filter holder with a PTFE membrane (Pall Corporation, NY). The volumetric flow rate was set to 10 Lpm. The mass of BCAgg (or BCPAgg) collected on the membrane was measured by a Cahn C-35 microbalance (Thermo Electron Corporation, MA).

The absorption coefficient (β_{abs}) and scattering coefficient (β_{sca}) were measured by five IPN spectrometers operating at laser wavelengths of 375 nm, 405 nm, 532 nm, 671 nm, and 1047

nm, respectively. In a IPN spectrometer, pulses of light energy are absorbed by particles and increase their temperature. Heat is conducted from the particle to the surrounding air, thereby expanding the air and creating a pressure disturbance or sound wave. This sound waves, which can be measured by a frequency-modulated, highly sensitive microphone, is directly proportional to the amount of light absorbed by the particles.
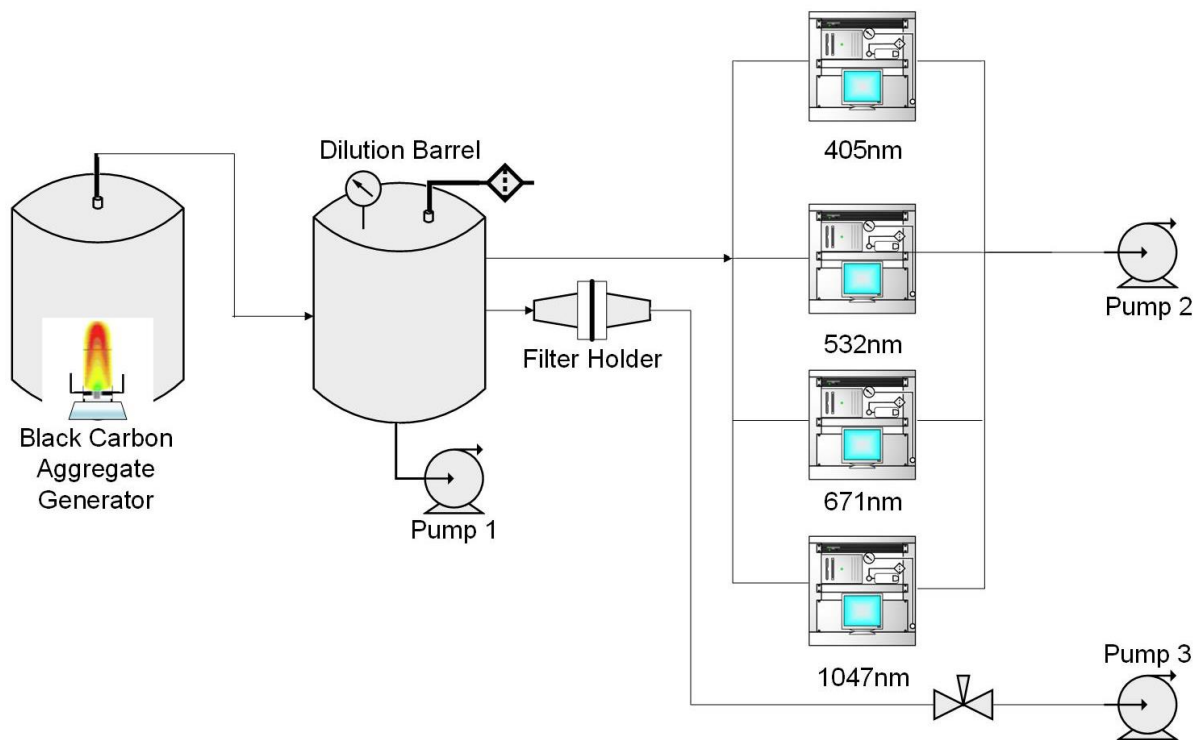
Figure 3.12 Schematic diagram of experimental set-up for BCAgg characterization

3.4.2 Experimental Set-up for Black Carbon Percolated Aggregate (BCPAgg) Measurements

The experimental set-up for Black Carbon Percolated Aggregates (BCPAgg) is shown in fig. 3.13. The BCPAgg Generator set-up has been illustrated by Pai et al[79]. A Burke-Schumann type coflow diffusion flame burner was operated in down-fired configuration. The burner consists of two concentric stainless steel tubes with 16 and 70 mm inner diameters,

respectively. A honeycomb flow straightener was placed to straighten the coflow stream. A 70 mm outer diameter quartz tube sheathed the burner to stabilize the flame. Ethylene (C_2H_4) served as the fuel for this work was delivered through the central tube with a volumetric flow rate 3.5 Lpm. oxygen (O_2) and nitrogen (N_2) were mixed and delivered though the annular tube of the burner at volumetric flow rates were 10 and 20, Lpm respectively. A sample collector was placed under the flame outflow region collect the falling BCPAgg particles. After approximately 10 minutes, the burner was turned off and disconnected from the sample collector. A 15 psi compressed air supply was connected to the collector and propelled BCPAgg particles into a resuspension chamber, breaking the aggregates into smaller particles. The resuspension chamber was connected to the measurement system in the location formerly occupedy be the dilution barrel. The PTFE filter remained in place and pumps 1 and 2 operated as before.

Measurements of the BCPAgg size distribution and morphology were conducted by using a microanalysis particle sampler (Model MPS-3, California Measurements Inc, Sierra Madre, CA) with a sampler for SEM analysis on each stage. The volumetric flow rate was set as 2 Lpm with a 1:19 dilution. The size distribution was obtained from processing the SEM images from the samplers using MATLAB code.
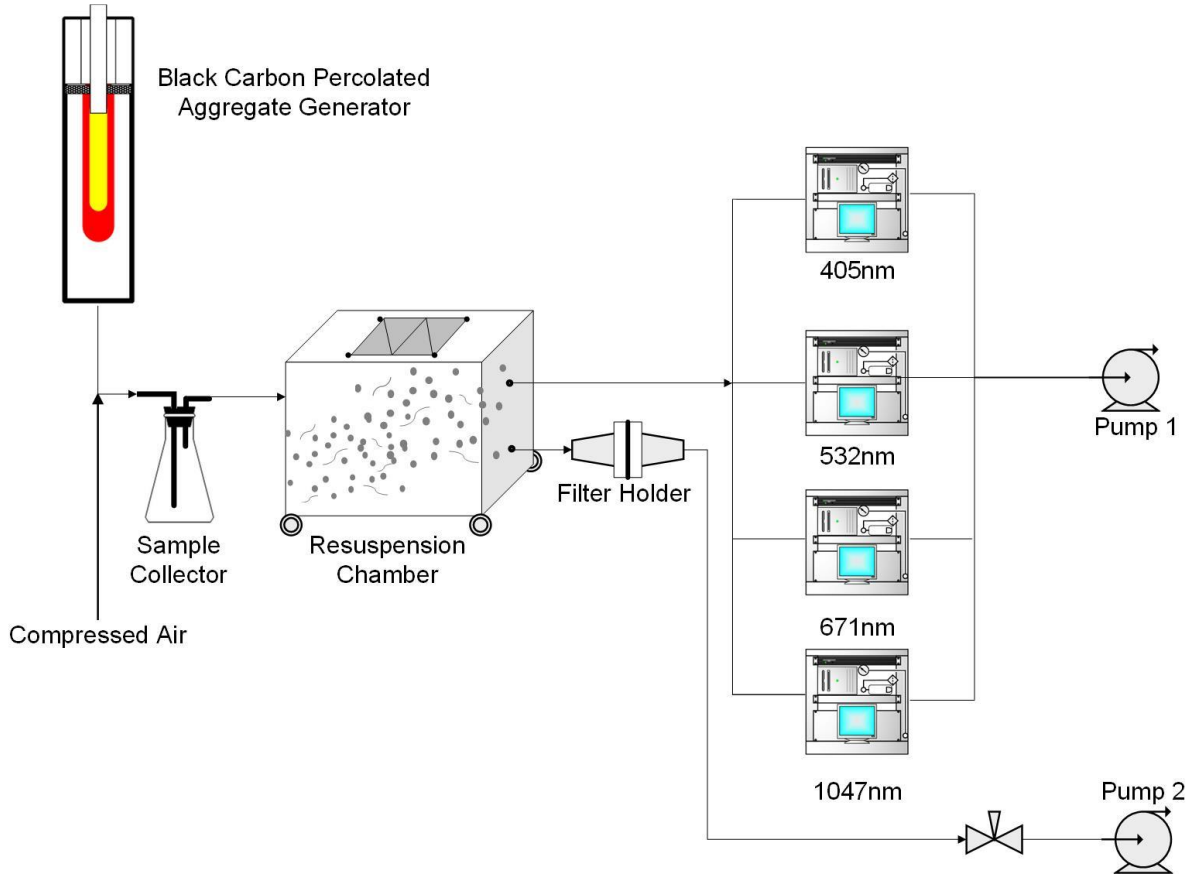
Figure 3.13 Schematic diagram of experimental set-up for: BCPAgg characterization

3.4.3 Calculation of Mass Absorption Cross-section (MAC), Mass Scattering Cross-section and Mass Extinction Cross-section

The mass absorption cross-section (MAC), measured in m^2/g, was determined by dividing the absorption coefficients by the particle concentration. MAC is an important variable representing absorption in radiative-transfer models. Theoretically, MAC can be calculated for each aerosol type using Mie theory, particle size, mixing state, and refractive index.[35] In this study, MAC was calculated as

$$MAC\left(\frac{m^2}{g}\right) = \frac{\beta_{abs}}{\rho} = \beta_{abs}(mm^{-1})\frac{f_v\left(\frac{m^3}{s}\right)}{f_m\left(\frac{g}{s}\right)}, \tag{3.22}$$

where ρ is the density of particle, f_v is the Volumatic flow rate and f_m is the mass flow rate.

3.4.4   Morphology of BCAgg and BCPAgg

Black carbon aggregate (BCAgg) is obtained during the combustion of kerosene when oxygen is insufficient for complete combustion. A complex series of reactions forms the precursors of BCAgg. In the STEM image in Fig. 3.14, a BCAgg particle displays predominantly chain agglomerates, with spherical primary particles of ≈ 10 nm diameter clearly discernible.
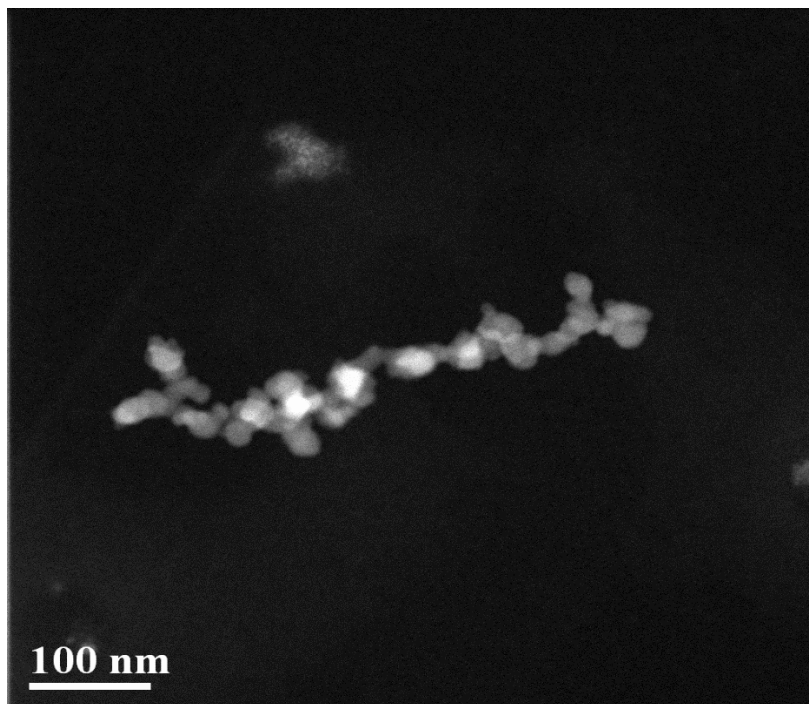
Figure 3.14 STEM image of black carbon aggregate (BCAgg)

Black carbon Percolated Aggregate (BCPAgg), shown in SEM image in Fig. 3.15 is formed from the percolation of carbon aggregates in the flame, and its size is around 20 microns. It retains the fractal structure with pores trapped inside.
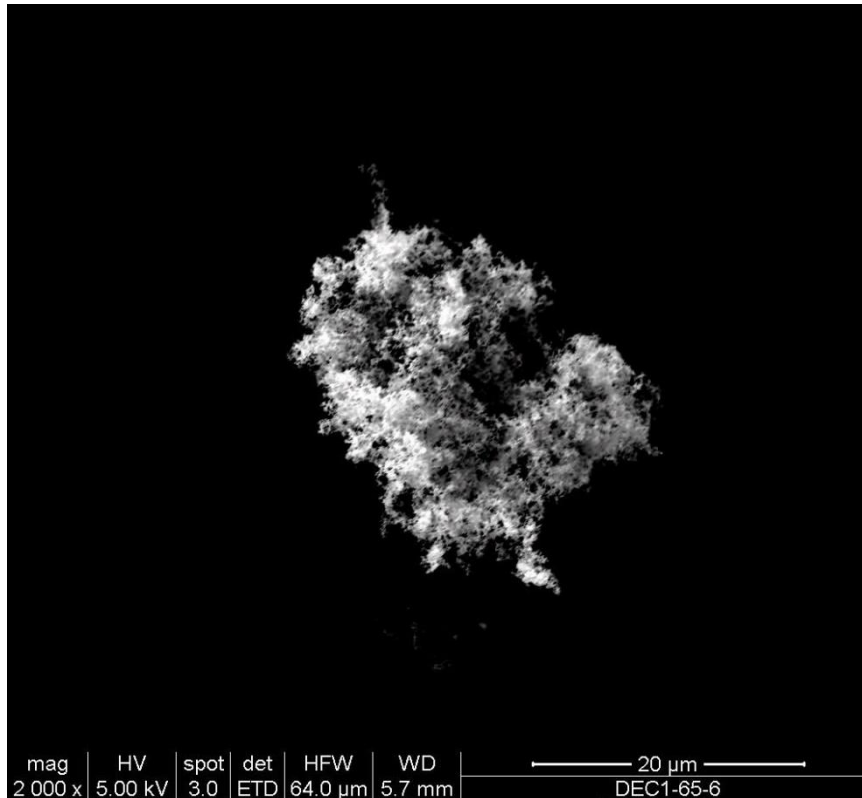
Figure 3.15 SEM image of black carbon percolated aggregate (BCPAgg)

3.4.5 Size distribution of BCAgg and BCPAgg

The size distribution of BCAgg was measured by Scanning Mobility Particle Sizer (Model 3938, TSI Inc, Shoreview, MN). The sheath flow rate was set at 3 lpm and the range of measurement was 10-750nm. Fig. 3.16a shows the size distribution function of BCAgg, for which the median, mean, geometric mean, and mode diameter are 272.14, 303.14, 258.39, and 315.99 nm, respectively. The size distribution of BCPAgg was obtained by the SEM sampler from the first two stages of microanalysis particle sampler (Model MPS-3, California Measurements Inc, Sierra Madre, CA) (Fig. 3.16b). For the first stage, the measurement range of the radius of gyration (Rg) was from 1 to 25μm, and the mean size was 9 μm. For the second stage, the range of Rg was between 0.25 and 6.75 μm while the mean size was 1.75μm.
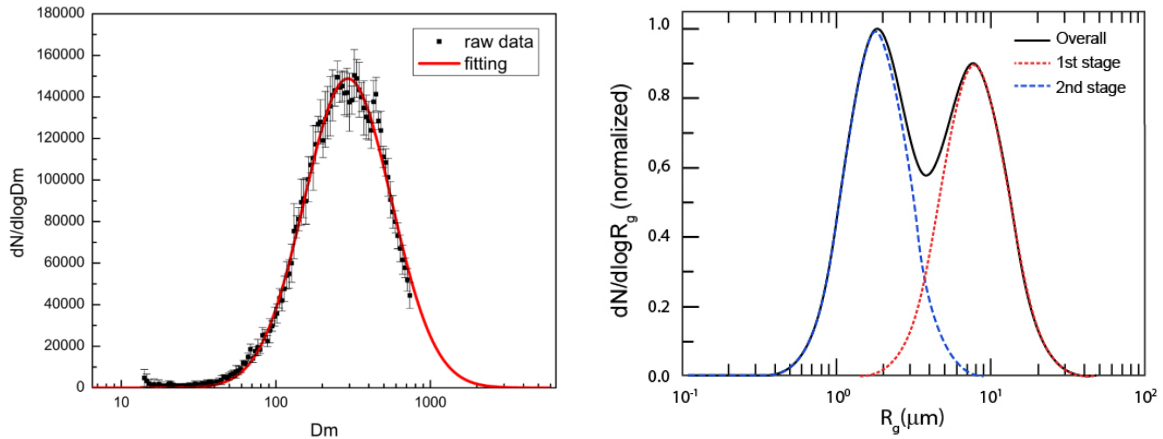
Figure 3.16 Size distribution for: (left) Black carbon aggregate (r) Black carbon percolated aggregate

3.4.6 Optical properties of BCAgg and BCPAgg

To compare the effect of wavelength on the optical properties of BC, we calculated the MAC of BCAgg and BCPAgg particles (Fig. 3.17). The Angstrom exponent was calculated for each parameter above to evaluate their wavelength dependence. The measurements were performed at $\lambda = 405, 532, 671$, and 1047 nm.
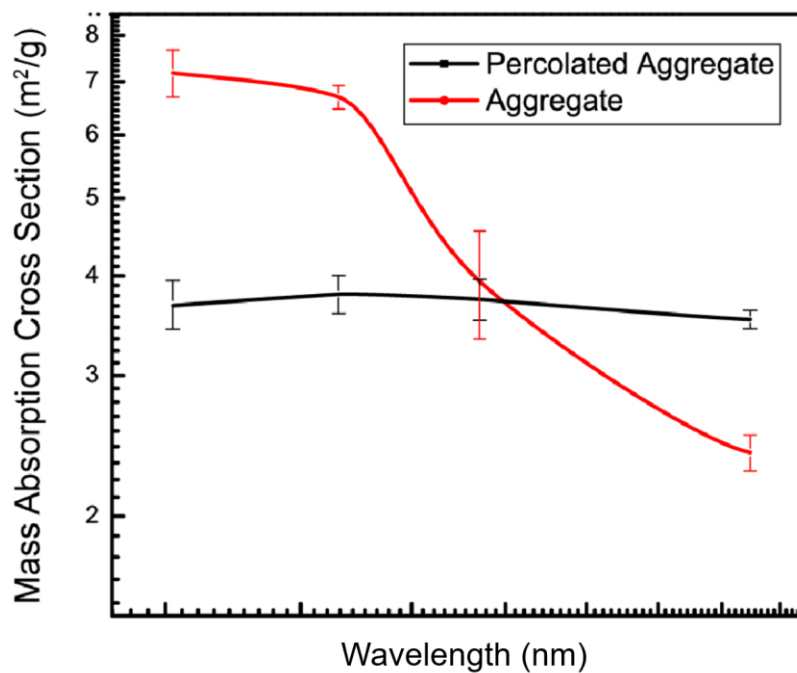
Figure 3.17 MAC plot for BCAgg and BCPAgg

The MAC value for BCAgg at λ = 405, 532, 671, and 1047 nm presents a decreasing trend which whose values are 7.13, 6.70, 3.93, and 2.40 m^2/g, respectively. The Angstrom exponent is piecewise continuous. From 405 nm to 532 nm, the Angstrom exponent was 0.14. Then it increased to 2.29 between 532 nm and 671 nm, and finally dropped to 1.11 between 671 nm and 1047 nm.

In contrast to the results for BCAgg, the trend of the MAC value and its Angstrom exponent for BCPAgg were both flat. The MAC values at λ = 405, 532, 671, and 1047 nm were 3.68, 3.79, 3.74, and 3.52 m^2/g, respectively. The Angstrom exponent remained around 0.04 at all wavelengths.

3.4.7   Results and Discussion

In order to analyze experimental data, a series of simulation was performed. BCAgg particles were simulated using an off-lattice diffusion limited cluster-cluster aggregation (DLCA) algorithm. Numerous experimental studies have shown that DLCA accurately predicts the formation of real-world BCAgg. The DLCA simulations were performed in two configurations: monomer dilute in which aggregates developed with the dimension of $D_f=1.8$ and monomer dense that produced aggregates similar in nature to those made under site percolation with $D_f=2.5$. The $D_f=1.8$ aggregates are referred to as simply just aggregates and the $D_f=2.5$ aggregates are referred to BCPAgg particles.

The Maxwell-Garnet effective medium theory conveniently provides a way to calculate the effective complex index of refraction m_{eff} of inhomogeneous porous particles. A porous object

would have a significantly reduced m_{eff} compared to an equivalent sphere with homogeneous index m.   In the case of void-filled aggregates, the theory describes m_{eff} by the relation:

$$f_v \left(\frac{m^2 - 1}{m^2 + 2} \right) = \left(\frac{m_{eff}^2 - 1}{m_{eff}^2 + 2} \right), \tag{3.23}$$

where f_v is the fraction of the particle volume filled. Based on the Bond et al.[30], refractive index homogeneous BC, monomer index was set $m=1.96+0.79i$. For simulated aggregates f_v is found by aligning the aggregates along the principal axis and constructing the smallest inclosing ellipsoid and then f_v is the ratio of the volumes of the aggregates constituent monomers to the volume of the containing ellipsoid. As shown in Fig. 3.18a the aggregates f_v scales with the mobility diameter D_m[µm] as:

$$f_v = 0.017 D_m^{-1.4}. \tag{3.24}$$

And in Fig. 3.18b f_v of the percolated aggregates scales as:

$$f_v = 0.045 D_m^{-0.55}. \tag{3.25}$$

By using the equations for f_v in the expression for the complex m_{eff}, the real m_{Re} and complex m_{Im} parts of m_{eff} for aggregates and percolated aggregates are presented in Figs. 3.18c and d respectively. The m_{Im} and m_{Re}-1 scale as a power with D_m. For the aggregates m_{Im} and m_{Re}-1 follow a -1.39 exponent while the percolated aggregates follow a -0.46 exponent.

The phase shift parameter ρ, accounts for the accumulated phase difference of light passing through a particle of refractive index m_{eff} and is defined as:

$$\rho = \frac{4\pi}{\lambda} R |m_{eff} - 1|, \tag{3.26}$$

where λ is the wave length of the incident light and R is the characteristic radius of the particle. ρ is used to predict the crossover between the Rayleigh optics when $\rho<1$ and geometric optics

when $\rho > 1$. For aggregates and percolated aggregates ρ is plotted versus D_m for in Figs. 3.18e

and f respectively.

For aggregates with $D_f = 1.8$ the phase shift scales with D_m as:

$$\rho = C_\lambda D_m^{-0.232},\tag{3.27}$$

where C_λ is a prefactor that decreases with increasing wavelength. As aggregates grow with

low $D_f < 2$ they become more void filled and thus ρ decreases with higher D_m. The percolated

aggregates have $D_f > 2$ and gain phase as they grow and scale with a power law with D_m as:

$$\rho = C_\lambda D_m^{0.45},\tag{3.28}$$

where C_λ again decreases with increasing wavelength.
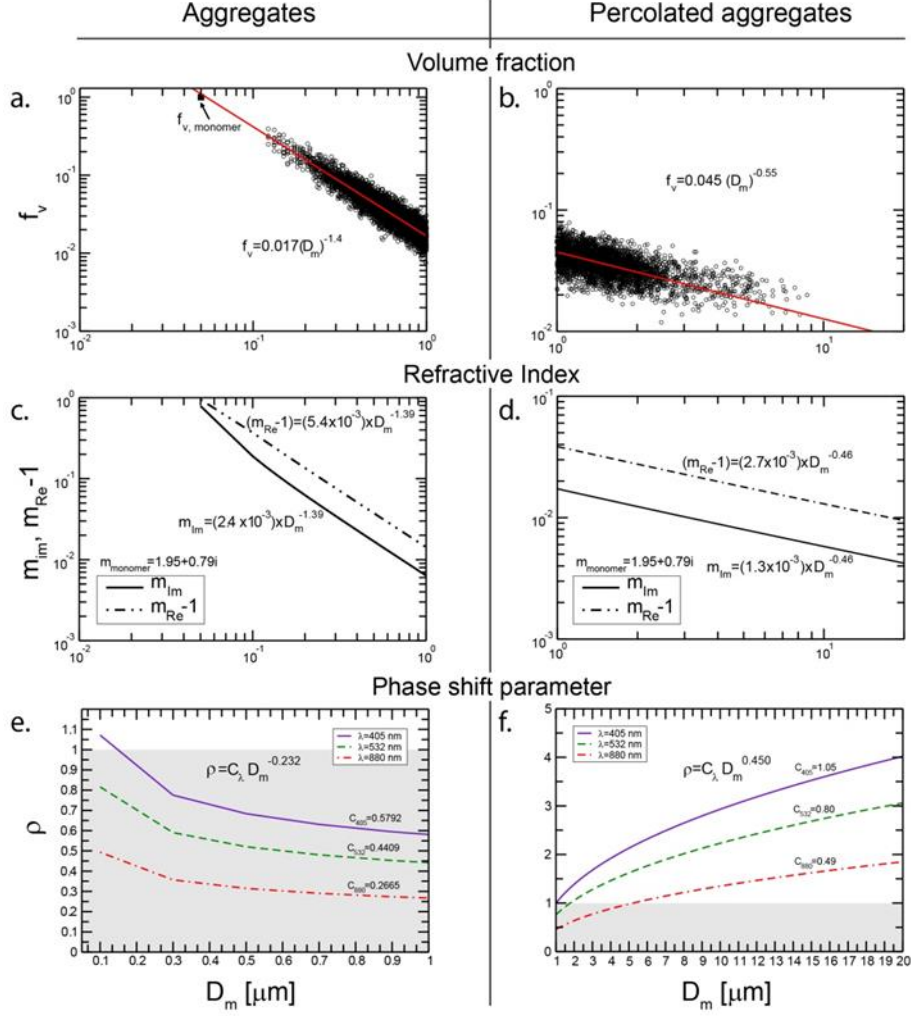
Figure 3.18 The volume fraction fv, effective refractive index meff and phase shift parameter ρ

for aggregates and percolated aggregates

The volume fraction in (a) for aggregates made in DLCA simulation scales as $f_v=0.017 \cdot D_m^{-1.4}$ which in turn leads to the components of the m_{eff} to scale with exponent of -1.39 in (c) and finally in (e) the phase shift follows the power law relation $\rho = C_\lambda D_m^{-0.232}$. Dense DLCA system produced percolated aggregates where their volume fraction in (b) goes as $f_v=0.045 \cdot D_m^{-0.5}$. The components of m_{eff} follow a power law with exponent of -0.45 in (d) and in (f) the phase shift follows the power law relation $\rho = C_\lambda D_m^{0.45}$.

The BCAgg's size distribution peaked at $D_m=200nm$ for $\lambda>405nm$ the aggregates have a $\rho<1$ at peak D_m while at $\lambda=405$ ρ approached unity. Assuming that aggregates are in the Rayleigh regime the absorption cross-section is then:

$$C_{abs} = N \cdot C_{abs,mono}, \tag{3.29}$$

Where N is the number of monomers in the aggregate and $C_{abs, mono}$ is the absorption cross section for the monomer. The mass absorption cross section (MAC) is the particle C_{abs} divided by particle mass which for Rayleigh particles becomes:

$$MAC = \frac{N \cdot C_{abs,mono}}{N \cdot m_{mono}} = \frac{C_{abs,mono}}{m_{mono}} = MAC_{mono}. \tag{3.30}$$

In the Rayleigh regime the MAC of the aggregate is equal to the MAC value of the monomer. The $C_{abs,mono}$ for Rayleigh monomer is

$$C_{abs,mono} = 4\pi \frac{2\pi}{\lambda} a^3 Im\left(\frac{m^2 - 1}{m^2 + 2}\right), \tag{3.31}$$

where a is the monomer radius. Thus the spectral response for Rayleigh aggregate MAC values is expected to be:

$$MAC \propto \lambda^{-1}, \tag{3.32}$$

which matches the experimental collected for BCAgg particles.

The BCPAgg's size distribution peaked at $Dm=9\mu m$ for all three wavelengths the aggregates have a $\rho>1$ at peak. Thus, BCPAgg particles are in the geometric optics regime and their spectral response for MAC values is expected to be:

$$MAC \propto 2\pi R^2, \tag{3.33}$$

which means the MAC values is related to the diffraction cross-section of the particles and it is not wavelength dependent. This theoretical reasoning is in line with the observation of flat trend observed for BCPAgg experimental data.

4   Conclusions

I assembled an integrated photoacoustic-nephelometer (IPN) spectrometer operated in the near-IR (1047 nm) wavelength. Laser alignment, scattering, and absorption calibration were performed comprehensively on this instrument. The instrument staility and dectection limit was evaluated using the Allan deviation method. Results showed that this spectrometer's measurements could be considered drift-free and stable after it has undergone a long initial warm up. The detection limits for absorption and scattering coefficients were 1.15 and 40.14 Mm^{-1}, respectively.

In order to evaluate the instrument performance during aircraft measurements, pressure sensitity analysis was performed. Comparing our experimental data with model predictions, it was found that the instrument performance is adequate and characterized well for accurate measurements of the aerosol absorption and scattering coefficients with ambient pressure higher than 700 mb. At pressures lower than this value, the measurements started to deviate up to 20%.

The instrument performance was evaluated by measuring the optical properties of fractal black carbon aggregates (BCAgg) and peroclated aggregates (BCPAgg). The IPN was co-located with three other IPN spectrometers operated at 405, 532 and 671 nm, respectively during this measurement. Dipole-dipole Approximation electromagnetic simulation for the MAC values of BCAgg and BCPAgg was used to explain the experimetal data. The result showed that BCAgg particles were in Rayleigh regime, with $MAC \propto \lambda^{-1}$, while BCPAgg

particles were in the geometric regime with $MAC \propto 2\pi R^2$. The experimental findings compared very well with the theoretical predictions.

References

1.	Abel, S. J.; Haywood, J. M.; Highwood, E. J.; Li, J.; Buseck, P. R., Evolution of biomass burning aerosol properties from an agricultural fire in southern Africa. *Geophysical Research Letters* **2003,** *30,* (15).

2.	Bond, T. C.; Doherty, S. J.; Fahey, D.; Forster, P.; Berntsen, T.; DeAngelo, B.; Flanner, M.; Ghan, S.; Kärcher, B.; Koch, D., Bounding the role of black carbon in the climate system: A scientific assessment. *Journal of Geophysical Research: Atmospheres* **2013,** *118,* (11), 5380-5552.

3.	Flowers, E.; McCormick, R.; Kurfis, K., Atmospheric turbidity over the United States, 1961-1966. *Journal of Applied Meteorology* **1969,** *8,* (6), 955-962.

4.	Johnson, D. L.; Allegre, R.; Burhrman, E.; Miller, S.; Sheldon, M.; Rosen, A., Air Pollution:" Public Attitudes and Public Action". *The American Behavioral Scientist* **1972,** *15,* (4), 533.

5.	Miller, M.; Friedlander, S.; Hidy, G., A chemical element balance for the Pasadena aerosol. *Journal of Colloid and Interface Science* **1972,** *39,* (1), 165-176.

6.	Rosen, H.; Novakov, T., Identification of primary particulate carbon and sulfate species by Raman spectroscopy. *Atmospheric Environment (1967)* **1978,** *12,* (4), 923-927.

7.	Lin, C.-I.; Baker, M.; Charlson, R. J., Absorption coefficient of atmospheric aerosol: a method for measurement. *Applied Optics* **1973,** *12,* (6), 1356-1363.

8.	Yasa, Z.; Amer, N. M.; Rosen, H.; Hansen, A.; Novakov, T., Photoacoustic investigation of urban aerosol particles. *Applied Optics* **1979,** *18,* (15), 2528-2530.

9.	Grosjean, D.; Williams, E. L.; Grosjean, E.; Novakov, T., Evolved gas analysis of secondary organic aerosols. *Aerosol science and technology* **1994,** *21,* (4), 306-324.

10.	Huntzicker, J.; Johnson, R.; Shah, J.; Cary, R., Analysis of organic and elemental carbon in ambient aerosols by a thermal-optical method. In *Particulate Carbon*, Springer: 1982; pp 79-88.

11.	Chow, J. C.; Watson, J. G.; Pritchett, L. C.; Pierson, W. R.; Frazier, C. A.; Purcell, R. G., The DRI thermal/optical reflectance carbon analysis system: description, evaluation and

applications in US air quality studies. *Atmospheric Environment. Part A. General Topics* **1993,** *27*, (8), 1185-1201.

12. Jimenez, J.; Canagaratna, M.; Donahue, N.; Prevot, A.; Zhang, Q.; Kroll, J. H.; DeCarlo, P. F.; Allan, J. D.; Coe, H.; Ng, N., Evolution of organic aerosols in the atmosphere. *Science* **2009,** *326*, (5959), 1525-1529.

13. Rosen, H.; Novakov, T.; Bodhaine, B., Soot in the Arctic. *Atmospheric Environment (1967)* **1981,** *15*, (8), 1371-1374.

14. Rosen, H.; Hansen, A., Role of combustion-generated carbon particles in the absorption of solar radiation in the Arctic haze. *Geophysical research letters* **1984,** *11*, (5), 461-464.

15. Doherty, S.; Warren, S.; Grenfell, T.; Clarke, A.; Brandt, R., Light-absorbing impurities in Arctic snow. *Atmospheric Chemistry and Physics* **2010,** *10*, (23), 11647-11680.

16. Harren, F. J.; Mandon, J.; Cristescu, S. M., Photoacoustic spectroscopy in trace gas monitoring. *Encyclopedia of Analytical Chemistry* **2000**.

17. Novakov, T.; Andreae, M.; Gabriel, R.; Kirchstetter, T.; Mayol-Bracero, O.; Ramanathan, V., Origin of carbonaceous aerosols over the tropical Indian Ocean: Biomass burning or fossil fuels. *Geophys. Res. Lett* **2000,** *27*, (24), 4061-4064.

18. Arnott, W. P.; Moosmüller, H.; Walker, J. W., Nitrogen dioxide and kerosene-flame soot calibration of photoacoustic instruments for measurement of light absorption by aerosols. *Review of Scientific Instruments* **2000,** *71*, (12), 4545-4552.

19. Lim, S.; Lee, M.; Kim, S.-W.; Yoon, S.-C.; Lee, G.; Lee, Y., Absorption and scattering properties of organic carbon versus sulfate dominant aerosols at Gosan climate observatory in Northeast Asia. *Atmospheric Chemistry and Physics* **2014,** *14*, (15), 7781-7793.

20. Petzold, A.; Ogren, J.; Fiebig, M.; Laj, P.; Li, S.-M.; Baltensperger, U.; Holzer-Popp, T.; Kinne, S.; Pappalardo, G.; Sugimoto, N., Recommendations for reporting" black carbon" measurements. *Atmospheric Chemistry and Physics* **2013,** *13*, (16), 8365-8379.

21. Cornelissen, G.; Gustafsson, Ö.; Bucheli, T. D.; Jonker, M. T.; Koelmans, A. A.; van Noort, P. C., Extensive sorption of organic compounds to black carbon, coal, and kerogen in sediments and soils: mechanisms and consequences for distribution, bioaccumulation, and biodegradation. *Environmental Science & Technology* **2005,** *39*, (18), 6881-6895.

22. Brodowski, S.; Amelung, W.; Haumaier, L.; Abetz, C.; Zech, W., Morphological and chemical properties of black carbon in physical soil fractions as revealed by scanning electron microscopy and energy-dispersive X-ray spectroscopy. *Geoderma* **2005,** *128*, (1), 116-129.

23. Mandelbrot, B. B., *Fractals*. Wiley Online Library: 1977.

24. Heinson, W. R. Simulation studies on shape and growth kinetics for fractal aggregates in aerosol and colloidal systems. Kansas State University, 2015.

25. Sorensen, C., The mobility of fractal aggregates: a review. *Aerosol Science and Technology* **2011,** *45*, (7), 765-779.

26. Sorensen, C., Light scattering by fractal aggregates: a review. *Aerosol Science & Technology* **2001,** *35*, (2), 648-687.

27. Kolb, M.; Herrmann, H. J., The sol-gel transition modelled by irreversible aggregation of clusters. *Journal of Physics A: Mathematical and General* **1985,** *18*, (8), L435.

28. Family, F.; Meakin, P.; Vicsek, T., Cluster size distribution in chemically controlled cluster–cluster aggregation. *The Journal of chemical physics* **1985,** *83*, (8), 4144-4150.

29. Sorensen, C.; Chakrabarti, A., The sol to gel transition in irreversible particulate systems. *Soft Matter* **2011,** *7*, (6), 2284-2296.

30. Bond, T. C.; Bergstrom, R. W., Light absorption by carbonaceous particles: An investigative review. *Aerosol science and technology* **2006,** *40*, (1), 27-67.

31. Antonov, V.; Antonov, V. N.; Jepsen, O.; Andersen, O.; Borghesi, A.; Bosio, C.; Marabelli, F.; Piaggi, A.; Guizzetti, G.; Nava, F., Optical properties of WSi 2. *Physical Review B* **1991,** *44*, (16), 8437.

32. Moosmüller, H.; Chakrabarty, R.; Ehlers, K.; Arnott, W., Absorption Ångström coefficient, brown carbon, and aerosols: basic concepts, bulk matter, and spherical particles. *Atmospheric Chemistry and Physics* **2011,** *11*, (3), 1217-1225.

33. Bergstrom, R. W.; Pilewskie, P.; Russell, P.; Redemann, J.; Bond, T.; Quinn, P.; Sierau, B., Spectral absorption properties of atmospheric aerosols. *Atmospheric Chemistry and Physics* **2007,** *7*, (23), 5937-5943.

34. Kirchstetter, T. W.; Novakov, T.; Hobbs, P. V., Evidence that the spectral dependence of light absorption by aerosols is affected by organic carbon. *Journal of Geophysical Research: Atmospheres* **2004,** *109*, (D21).

35. Lack, D.; Cappa, C., Impact of brown and clear carbon on light absorption enhancement, single scatter albedo and absorption wavelength dependence of black carbon. *Atmospheric Chemistry and Physics* **2010,** *10*, (9), 4207-4220.

36. Zhang, Q.; Jimenez, J.; Canagaratna, M.; Allan, J.; Coe, H.; Ulbrich, I.; Alfarra, M.; Takami, A.; Middlebrook, A.; Sun, Y., Ubiquity and dominance of oxygenated species in organic aerosols in anthropogenically-influenced Northern Hemisphere midlatitudes. *Geophysical Research Letters* **2007,** *34*, (13).

37. Yang, M.; Howell, S.; Zhuang, J.; Huebert, B., Attribution of aerosol light absorption to black carbon, brown carbon, and dust in China–interpretations of atmospheric measurements during EAST-AIRE. *Atmospheric Chemistry and Physics* **2009,** *9*, (6), 2035-2050.

38. Haywood, J.; Shine, K., The effect of anthropogenic sulfate and soot aerosol on the clear sky planetary radiation budget. *Geophysical Research Letters* **1995,** *22*, (5), 603-606.

39. Chylek, P.; Wong, J., Effect of absorbing aerosols on global radiation budget. *Geophysical Research Letters* **1995,** *22*, (8), 929-931.

40. Tam, A. C., Applications of photoacoustic sensing techniques. *Reviews of Modern Physics* **1986,** *58*, (2), 381.

41. Raspet, R.; Slaton, W. V.; Arnott, W. P.; Moosmüller, H., Evaporation-condensation effects on resonant photoacoustics of volatile aerosols. *Journal of Atmospheric and Oceanic Technology* **2003,** *20*, (5), 685-695.

42. Chan, C., Effective absorption for thermal blooming due to aerosols. *Applied Physics Letters* **1975,** *26*, (11), 628-630.

43. Arnott, W.; MOOSMÜLLER, H.; Sheridan, P.; Ogren, J.; Raspet, R.; Slaton, W.; Hand, J.; Kreidenweis, S.; COLLETT, J., Photoacoustic and filter-based ambient aerosol light absorption measurements: Instrument comparisons and the role of relative humidity. *Journal of geophysical research* **2003,** *108*, (D1), AAC15. 1-AAC15. 11.

44. Gerlach, R.; Amer, N., Brewster window and windowless resonant spectrophones for intracavity operation. *Applied physics* **1980,** *23*, (3), 319-326.

45. Sedlacek, A.; Lee, J., Photothermal interferometric aerosol absorption spectrometry. *Aerosol Science and Technology* **2007,** *41*, (12), 1089-1101.

46. Petzold, A.; Kramer, H.; Schönlinner, M., Continuous measurement of atmospheric black carbon using a multi-angle absorption photometer. *Environ. Sci. Pollut. Res* **2002,** *4*, (Special Issue), 78-82.

47. Petzold, A.; Rasp, K.; Weinzierl, B.; Esselborn, M.; Hamburger, T.; Dörnbrack, A.; Kandler, K.; Schütz, L.; Knippertz, P.; Fiebig, M., Saharan dust absorption and refractive index from aircraft-based observations during SAMUM 2006. *Tellus B* **2009,** *61*, (1), 118-130.

48. Moosmüller, H.; Arnott, W.; Rogers, C., Methods for real-time, in situ measurement of aerosol light absorption. *Journal of the Air & Waste Management Association* **1997,** *47*, (2), 157-166.

49. Campillo, A. J.; Dodge, C. J.; Lin, H.-B., Aerosol particle absorption spectroscopy by photothermal modulation of Mie scattered light. *Applied optics* **1981,** *20*, (18), 3100-3103.

50. Arnott, W. P.; Moosmüller, H.; Rogers, C. F.; Jin, T.; Bruch, R., Photoacoustic spectrometer for measuring light absorption by aerosol: instrument description. *Atmospheric Environment* **1999,** *33*, (17), 2845-2852.

51. Arnott, W.; Zielinska, B.; Rogers, C.; Sagebiel, J.; Park, K.; Chow, J.; Moosmüller, H.; Watson, J. G.; Kelly, K.; Wagner, D., Evaluation of 1047-nm photoacoustic instruments and photoelectric aerosol sensors in source-sampling of black carbon aerosol and particle-bound PAHs from gasoline and diesel powered vehicles. *Environmental science & technology* **2005,** *39*, (14), 5398-5406.

52. Ku, J. C.; Shim, K.-H., A comparison of solutions for light scattering and absorption by agglomerated or arbitrarily-shaped particles. *Journal of Quantitative Spectroscopy and Radiative Transfer* **1992,** *47*, (3), 201-220.

53. Michelsen, H. A., Understanding and predicting the temporal response of laser-induced incandescence from carbonaceous particles. *The Journal of chemical physics* **2003,** *118*, (15), 7012-7045.

54. Gerber, H., Portable cell for simultaneously measuring the coefficients of light scattering and extinction for ambient aerosols. *Applied optics* **1979,** *18*, (7), 1009-1014.

55. Weiss, R. E.; Waggoner, A. P.; Charlson, R. J.; Thorsell, D. L.; Hall, J.; Riley, L. In *Studies of the optical, physical and chemical properties of light absorbing aerosols*, Proceedings: Conference on Carbonaceous Particles in the Atmosphere, 1979; Document# LBL-9037, Lawrence Berkeley Laboratory, Berkeley, CA: 1979; p 257.

56. Weiss, R. E.; Hobbs, P. V., Optical extinction properties of smoke from the Kuwait oil fires. *Journal of Geophysical Research: Atmospheres* **1992,** *97*, (D13), 14537-14540.

57. Weiss, E.; Eck, T. F., Comparisons of techniques for measuring shortwave absorption and black carbon content of aerosols from biomass burning in Brazil. *Journal of Geophysical Research* **1998,** *103*, (D24), 32,031-32,040.

58. Laursen, K. K.; Ferek, R. J.; Hobbs, P. V.; Rasmussen, R. A., Emission factors for particles, elemental carbon, and trace gases from the Kuwait oil fires. *Journal of Geophysical Research: Atmospheres* **1992,** *97*, (D13), 14491-14497.

59. Virkkula, A.; Ahlquist, N. C.; Covert, D. S.; Sheridan, P. J.; Arnott, W. P.; Ogren, J. A., A three-wavelength optical extinction cell for measuring aerosol light extinction and its application to determining light absorption coefficient. *Aerosol science and technology* **2005,** *39*, (1), 52-67.

60. Sheridan, P. J.; Arnott, W. P.; Ogren, J. A.; Andrews, E.; Atkinson, D. B.; Covert, D. S.; Moosmüller, H.; Petzold, A.; Schmid, B.; Strawa, A. W., The Reno Aerosol Optics Study: An evaluation of aerosol absorption measurement methods. *Aerosol Science and Technology* **2005,** *39*, (1), 1-16.

61. Schnaiter, M.; Schmid, O.; Petzold, A.; Fritzsche, L.; Klein, K.; Andreae, M.; Helas, G.; Thielmann, A.; Gimmler, M.; Möhler, O., Measurement of wavelength-resolved light absorption by aerosols utilizing a UV-VIS extinction cell. *Aerosol science and technology* **2005,** *39*, (3), 249-260.

62. Moosmüller, H.; Varma, R.; Arnott, W. P., Cavity ring-down and cavity-enhanced detection techniques for the measurement of aerosol extinction. *Aerosol Science and Technology* **2005,** *39*, (1), 30-39.

63. Strawa, A. W.; Castaneda, R.; Owano, T.; Baer, D. S.; Paldus, B. A., The measurement of aerosol optical properties using continuous wave cavity ring-down techniques. *Journal of Atmospheric and Oceanic Technology* **2003,** *20*, (4), 454-465.

64. Thompson, J. E.; Barta, N.; Policarpio, D.; DuVall, R., A fixed frequency aerosol albedometer. *Optics express* **2008,** *16*, (3), 2191-2205.

65. Chen, L.-W. A.; Moosmüller, H.; Arnott, W. P.; Chow, J. C.; Watson, J. G.; Susott, R. A.; Babbitt, R. E.; Wold, C. E.; Lincoln, E. N.; Hao, W. M., Emissions from laboratory combustion of wildland fuels: Emission factors and source profiles. *Environmental science & technology* **2007,** *41*, (12), 4317-4325.

66. Abo Riziq, A.; Trainic, M.; Erlick, C.; Segre, E.; Rudich, Y., Extinction efficiencies of coated absorbing aerosols measured by cavity ring down aerosol spectrometry. *Atmospheric Chemistry and Physics* **2008,** *8*, (6), 1823-1833.

67. Butler, T.; Miller, J. L.; Orr-Ewing, A. J., Cavity ring-down spectroscopy measurements of single aerosol particle extinction. I. The effect of position of a particle within the laser beam on extinction. *The Journal of chemical physics* **2007,** *126*, (17), 174302-174302.

68. Miller, J. L.; Orr-Ewing, A. J., Cavity ring-down spectroscopy measurement of single aerosol particle extinction. II. Extinction of light by an aerosol particle in an optical cavity excited by a cw laser. *The Journal of chemical physics* **2007,** *126*, (17), 174303.

69. Sanford, T. J.; Murphy, D. M.; Thomson*, D. S.; Fox, R. W., Albedo measurements and optical sizing of single aerosol particles. *Aerosol Science and Technology* **2008,** *42*, (11), 958-969.

70. Moosmüller, H.; Arnott, W. P., Angular truncation errors in integrating nephelometry. *Review of scientific instruments* **2003,** *74*, (7), 3492-3501.

71. Allan, D. W., Statistics of atomic frequency standards. *Proceedings of the IEEE* **1966,** *54*, (2), 221-230.

72. Witt, T. J., Allan variances and spectral densities for DC voltage measurements with polarity reversals. *Instrumentation and Measurement, IEEE Transactions on* **2005,** *54*, (2), 550-553.

73. Levine, J., Introduction to time and frequency metrology. *Review of scientific instruments* **1999,** *70*, (6), 2567-2596.

74. Riley, W., *Handbook of Frequency*. NIST: 2008.

75. Czerwinski, F.; Richardson, A. C.; Oddershede, L. B., Quantifying noise in optical tweezers by allan variance. *Optics express* **2009,** *17*, (15), 13255-13269.

76. Nakayama, T.; Suzuki, H.; Kagamitani, S.; Ikeda, Y.; Uchiyama, A.; Matsumi, Y., Characterization of a three wavelength photoacoustic soot spectrometer (PASS-3) and a photoacoustic extinctiometer (PAX). 気象集誌. 第 2 輯 **2015,** *93*, (2), 285-308.

77. Sharma, N.; Arnold, I.; Moosmüller, H.; Arnott, W.; Mazzoleni, C., Photoacoustic and nephelometric spectroscopy of aerosol optical properties with a supercontinuum light source. *Atmospheric Measurement Techniques* **2013,** *6*, (12), 3501-3513.

78. Arnott, W. P.; Walker, J. W.; Moosmüller, H.; Elleman, R. A.; Jonsson, H. H.; Buzorius, G.; Conant, W. C.; Flagan, R. C.; Seinfeld, J. H., Photoacoustic insight for aerosol light absorption aloft from meteorological aircraft and comparison with particle soot absorption photometer measurements: DOE Southern Great Plains climate research facility and the coastal stratocumulus imposed perturbation experiments. *Journal of Geophysical Research: Atmospheres* **2006,** *111*, (D5).

79. Liu, P.; Arnold, I. J.; Wang, Y.; Yu, Y.; Fang, J.; Biswas, P.; Chakrabarty, R. K., Synthesis of Titanium Dioxide Aerosol Gels in a Buoyancy-Opposed Flame Reactor. *Aerosol Science and Technology* **2015,** *49*, (12), 1232-1241.

Appendix

MATLAB code for Allan Deviation calculation

function [avar]=allan(data, tau)

% Compute various Allan deviations for a constant-rate time series
% [AVAR]=allan(DATA, TAU)
%
% INPUTS:
% DATA should be a struct and has the following fields:
%   DATA.freq   the time series measurements in arb. units
%   DATA.rate   constant rate of time series in (Hz)
%   (Differently from previous versions of allan.m,
%   it is not possible to compute variances for time-
%   stamp data anymore.)
% TAU is an array of the tau values for computing Allan deviations
%
% OUTPUTS:
% AVAR is a struct and has the following fields (for values of tau):
%   AVAR.sig   = standard deviation
%   AVAR.sig2   = Allan deviation
%   AVAR.sig2err = standard error of Allan deviation
%   AVAR.osig   = Allan deviation with overlapping estimate
%   AVAR.osigerr = standard error of overlapping Allan deviation
%   AVAR.msig   = modified Allan deviation
%   AVAR.msigerr = standard error of modified Allan deviation
%   AVAR.tsig   = timed Allan deviation
%   AVAR.tsigerr = standard error of timed Allan deviation
%   AVAR.tau1   = measurement interval in (s)
%   AVAR.tauerr   = errors in tau that might occur because of initial
%   rounding
%
% NOTES:
% Calculations of modified and timed Allan deviations for very long time
% series become very slow. It is advisable to uncomment .msig* and .tsig*
% only after calculations of .sig*, .sig2* and .osig* have been proven
% sufficiently fast.
%
% No pre-processing of the data is performed.
% For constant-rate time series, the deviations are only calculated for tau

% values greater than the minimum time between samples and less than half
% the total time.
%
% versionstr = 'allan v3.0';
% FCz OCT2009
% v3.0   faster and very plain code, no plotting; various Allan deviations
%   can be calculated; script and sample data are availabie on
%   www.nbi.dk/~czerwin/files/allan.zip
%   (Normal, overlapping and modified Allan deviations are calculated in one
function,
%   in strong contrast to MAHs approach of splitting up among various functions.
This might be beneficial for individual cases though.)
%
% MAH 2009
% v2.0 and others
%
% FCz OCT2008
% v1.71 'lookfor' gives now useful comments; script and sample data are
%   availabie on www.nbi.dk/~czerwin/files/allan.zip
% v1.7   Improve program performance by mainly predefining matrices outside
%   of loops (avoiding memory allocation within loops); no changes to
%   manual
%
% early program core by Alaa MAKDISSI 2003
% (documentation might be found http://www.alamath.com/)
% revision and modification by Fabian CZERWINSKI 2009
% revision and modification by Yang Yu 2016
%
% For more information, see:
% [1] Fabian Czerwinski, Andrew C. Richardson, and Lene B. Oddershede,
% "Quantifying Noise in Optical Tweezers by Allan Variance,"
% Opt. Express 17, 13255-13269 (2009)
% http://dx.doi.org/10.1364/OE.17.013255

tau = (60:60: (60*324))';
data.rate = 1/60   % frequency
[num,txt,raw]=xlsread('C:\Users\Yang\Desktop\LASER.xlsx','671')   %example
data.freq = num (:,7)
% Load IPN data into MATLAB

n=length(data.freq);
jj=length(tau);
m=floor(tau*data.rate);

```matlab
avar.sig      = zeros(1, jj);
avar.sigerr   = zeros(1, jj);
avar.sig2     = (zeros(1, jj))';
avar.sig2err  = zeros(1, jj);
avar.osig     = (zeros(1, jj))';
avar.osigerr  = zeros(1, jj);
% avar.msig     = zeros(1, jj);
% avar.msigerr  = zeros(1, jj);
% avar.tsig     = zeros(1, jj);
% avar.msigerr  = zeros(1, jj);

tic;

for j=1:jj
    % fprintf('.');

    D=zeros(1,n-m(j)+1);
    D(1)=sum(data.freq(1:m(j)))/m(j);
    for i=2:n-m(j)+1
        D(i)=D(i-1)+(data.freq(i+m(j)-1)-data.freq(i-1))/m(j);
    end

    %standard deviation
    avar.sig(j)=std(D(1:m(j):n-m(j)+1));
    avar.sigerr(j)=avar.sig(j)/sqrt(n/m(j));

    %normal Allan deviation
    avar.sig2(j)=sqrt(0.5*mean((diff(D(1:m(j):n-m(j)+1)).^2)));
    avar.sig2err(j)=avar.sig2(j)/sqrt(n/m(j));

    %overlapping Allan deviation
    z1=D(m(j)+1:n+1-m(j));
    z2=D(1:n+1-2*m(j));
    u=sum((z1-z2).^2);
    avar.osig(j)=sqrt(u/(n+1-2*m(j))/2);
    avar.osigerr(j)=avar.osig(j)/sqrt(n-m(j));

%       %modified Allan deviation
%       u=zeros(1,n+2-3*m(j));
%       z1=D(1:m(j));
%       z2=D(1+m(j):2*m(j));
%       for L=1:n+1-3*m(j)
%           u(L)=(sum(z2-z1))^2;
%           z1=z1-y(L)+y(L+m(j));
```

```matlab
%               z2=z2-y(L+m(j))+y(L+2*m(j));
%           end
%           avar.msigerr(j)=avar.msig(j)/sqrt(n-m(j));
%           uu=mean(u);
%           avar.msig(j)=sqrt(uu/2)/m(j);
%
%           %timed Allan deviation
%           avar.tsig(j)=tau(j)*avar.msig(j)/sqrt(3);
%           avar.tsigerr(j)=avar.tsig(j)/sqrt(n-m(j));

    % toc

end;


avar.tau1=m/data.rate;
avar.tauerr=tau-avar.tau1;

toc;
end
```